Cancer Cell

Article

IGSF11-VISTA is a critical and targetable immune checkpoint axis in diffuse midline glioma

Graphical abstract

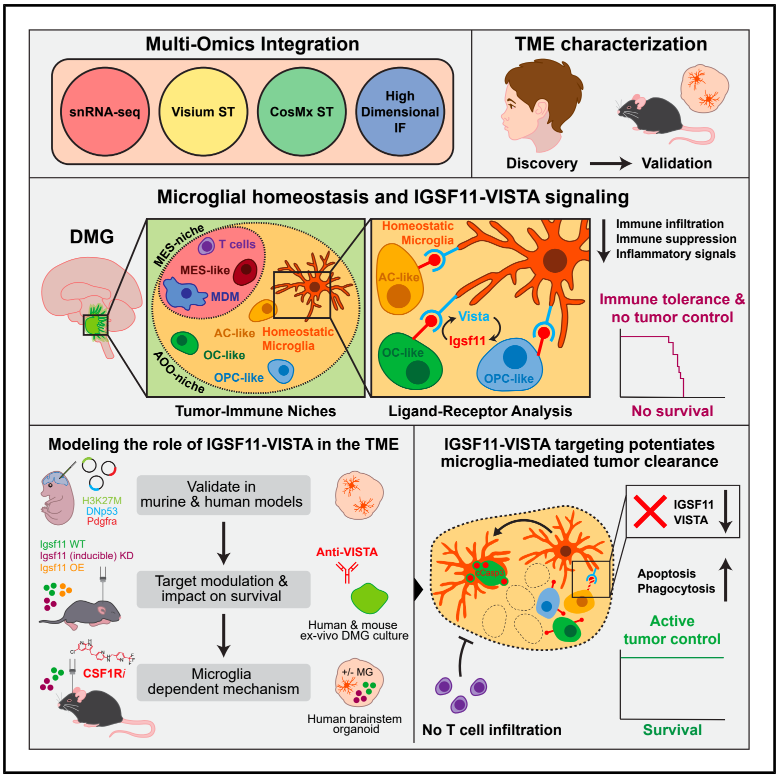

Highlights

- Spatial profiling identifies DMG tumor niches associated with homeostatic microglia
- Cancer cells in these areas express IGSF11 that signals through VISTA on microglia
- Targeting IGSF11-VISTA results in tumor clearance and prolonged survival
- Tumor control in the absence of IGSF11 is mediated by microglia and not T cells

Authors

Raphaël Collot, Cristian Ruiz-Moreno, Celina Honhoff, ..., Anoek Zomer, Hendrik G. Stunnenberg, Anne C. Rios

Correspondence

a.c.rios@prinsesmaximacentrum.nl

In brief

Collot et al. profile tumor and immune interactions in DMG. They identify DMG tumor cells that communicate with microglia through IGSF11-VISTA signaling. Targeting this communication pathway leads to tumor control by microglia and a favorable disease outcome. This positions IGS11-VISTA as a promising brain-specific therapeutic axis for DMG treatment.

Collot et al., 2026, Cancer Cell *44*, 1–17
March 9, 2026
https://doi.org/10.1016/j.ccell.2025.12.020

CellPress

Please cite this article in press as: Collot et al., IGSF11-VISTA is a critical and targetable immune checkpoint axis in diffuse midline glioma, Cancer Cell (2025), https://doi.org/10.1016/j.ccell.2025.12.020

Cancer Cell

CellPress
OPEN ACCESS

Article

IGSF11-VISTA is a critical and targetable immune checkpoint axis in diffuse midline glioma

Raphaël Collot,[1,2,10] Cristian Ruiz-Moreno,[1,3,10] Celina Honhoff,[1,2,10] Thijs J.M. van den Broek,[1,2] Amber K.L. Wezenaar,[1,2] Daan J. Kloosterman,[1,2] Hendrikus C.R. Ariese,[1,2] Hannah Johnson,[1,2] Britt M.T. Vervoort,[1,2] Amal Jeiroshi,[1] Jens Bunt,[1] Ravian L. van Ineveld,[1,2] Emma Bokobza,[1,2] Heggert G. Rebel,[1,2] Brigit M. te Pas,[1] Femke C.A. Ringnalda,[1,2] Marc van de Wetering,[1,2] Pierre A. Robe,[4] Marcel Kool,[1,5,6,7] Jennifer R. Cochran,[8] Mariëtte E.G. Kranendonk,[1] Dannis G. van Vuurden,[1] Esther Hulleman,[1] Ellen J. Wehrens,[1,2] Anoek Zomer,[1,2] Hendrik G. Stunnenberg,[1,3,11] and Anne C. Rios[1,2,9,11,12,*]

[1]Princess Máxima Center for Pediatric Oncology, Utrecht, the Netherlands
[2]Oncode Institute, Utrecht, the Netherlands
[3]Department of Molecular Biology, Faculty of Science, Radboud University, Nijmegen, the Netherlands
[4]Department of Neurology and Neurosurgery, Brain Center Rudolf Magnus, University Medical Center Utrecht, Utrecht, the Netherlands
[5]University Medical Center Utrecht, Utrecht, the Netherlands
[6]Hopp Children's Cancer Center (KiTZ), Heidelberg, Germany
[7]Division of Pediatric Neurooncology, German Cancer Research Center (DKFZ) and German Cancer Research Consortium (DKTK), Heidelberg, Germany
[8]Department of Bioengineering, Stanford University Schools of Engineering and Medicine, Stanford, CA, USA
[9]Department of Biology, Faculty of Science, Utrecht University, Utrecht, the Netherlands
[10]These authors contributed equally
[11]Senior author
[12]Lead contact
*Correspondence: a.c.rios@prinsesmaximacentrum.nl

https://doi.org/10.1016/j.ccell.2025.12.020

SUMMARY

Diffuse midline glioma (DMG) is an aggressive pediatric brain tumor with no curative treatment, and lacks a comprehensive understanding of immune-tumor cell interactions within their spatial context. Our multi-omics approach, integrating single-nuclei RNA sequencing, spatial transcriptomics, and high-dimensional imaging, utilizes patient samples and an experimental murine DMG model to unveil two spatially distinct regions. MES-patterns are defined by mesenchymal (MES) tumor cells and blood-derived immune cells, whereas AOO-patterns are enriched with astrocyte (AC)-, oligodendrocyte (OC)-, and oligodendrocyte precursor cell (OPC)-like cancer populations, alongside homeostatic-like microglia. The less-studied immune checkpoint, IGSF11, is primarily expressed by AOO-associated cancer cells, while its receptor VISTA is detected mainly in homeostatic microglia. Targeting IGSF11-VISTA results in tumor reduction and survival benefit, mediated by brain-resident microglia and independent of T cell infiltration. This positions IGSF11-VISTA as a promising immune checkpoint treatment axis to harness the local brain immune response against DMG.

INTRODUCTION

Diffuse midline glioma (DMG) is a highly aggressive pediatric brain tumor lacking curative treatments.[1–3] DMG is commonly characterized by a histone H3 lysine 27-to-methionine (H3K27M) mutation, predominantly the H3.3K27M variant.[4] This K27M mutation is often accompanied by mutations in oncogenes and tumor suppressor genes, with *TP53* mutations and *PDGFRA* amplification most frequently associated with H3.3K27M.[2,5] Recent single-cell studies have revealed diverse cancer cell states in DMG that show similarities to normal cells in the developing and adult brain, such as astrocytes (AC-like), oligodendrocytes (OC-like), and glioma cells arrested in a cancer stem cell-like oligodendrocyte precursor (OPC-like) state[6,7] as well as a mesenchymal (MES-like) identity reminiscent of adult glioblastoma (GB).[7–10] Together, these observations highlight critical cancer cell heterogeneity of DMG but also its reliance on developmental lineage programs, suggesting that co-opted developmental processes may represent therapeutic vulnerabilities.

Increasing attention has turned to the tumor microenvironment (TME) as a critical driver of DMG biology. The TME can be influenced by and, in turn, promote tumor heterogeneity[11]

Please cite this article in press as: Collot et al., IGSF11-VISTA is a critical and targetable immune checkpoint axis in diffuse midline glioma, Cancer Cell (2025), https://doi.org/10.1016/j.ccell.2025.12.020

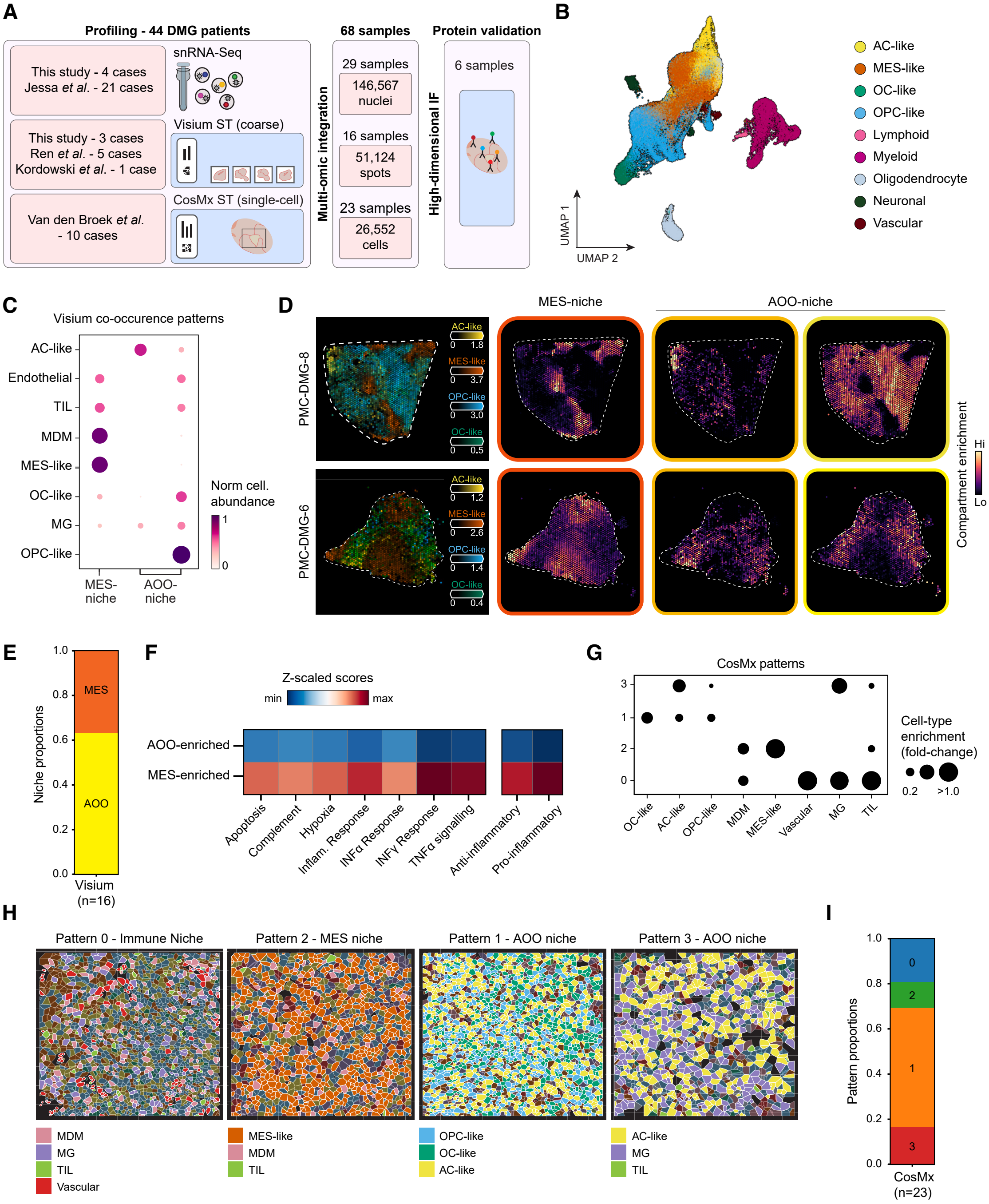

Figure 1. DMG spatially segregates into MES- and AOO-dominated tumor-immune niches

(A) Schematic depiction of human DMG patient and sample numbers across the different (spatial) transcriptomics and imaging modalities.

(B) UMAP visualization of main cell type clusters in snRNA-seq data from patients with DMG ($n = 25$).

(C) Dot plot representation of the co-occurrence patterns of tumor, immune, and environmental cells in Visium ST datasets ($n = 16$). Dot plot reflects estimated relative NMF weights normalized across components on a color and size scale.

(D) Representative Visium ST data depict the estimation of DMG cancer cell states abundance (color intensity) overlayed on top of the tissue image (left). Spatial representation of the co-occurrence patterns from C, shown as compartment enrichment (color intensity) with a dashed line delineating the tumor border (right).

(E) Stacked barplot depicts the relative contribution of MES- and AOO-enriched niche across Visium ST samples ($n = 16$).

(F) Heatmap visualization of z-scaled expression scores on a blue-to-red color gradient for biological and immune processes across AOO- and MES-enriched tumor areas ($n = 16$).

(legend continued on next page)

Please cite this article in press as: Collot et al., IGSF11-VISTA is a critical and targetable immune checkpoint axis in diffuse midline glioma, Cancer Cell (2025), https://doi.org/10.1016/j.ccell.2025.12.020

and critically contributes to glioma growth.[12–17] Especially in pediatric DMG, tumor-associated myeloid cells constitute a predominant component of the TME,[7,16] whereas T cells are scarce compared to GB.[18,19] These myeloid cells actively interact with tumor cells to create an immunosuppressive environment and sustain tumor growth.[20] Unraveling how myeloid and tumor cells co-localize will be essential to understand how DMG establishes a tumor-supportive immune environment and may reveal exploitable therapeutic vulnerabilities. Recent studies have identified specific receptor-ligand interactions that may contribute to tumor-myeloid cell communication and influence cancer cell maturation toward OPC-like and MES-like states.[7] This emphasizes the need for a deeper understanding of the spatial and molecular interplay between immune and tumor populations in DMG. The true extent and therapeutic relevance of these predicted interactions remain to be determined and require functional validation.

Here, we combined spatial transcriptomics with single-nuclei RNA sequencing and high-dimensional imaging to map the spatial distribution and interactions of DMG cell populations with immune cells in patient samples. We identified IGSF11-VISTA as a promising immune checkpoint axis between cancer cells in the developmental-like tumor regions and homeostatic-like microglia. Targeting this axis resulted in robust tumor elimination and a significant survival benefit, mediated by microglia.

RESULTS

Multimodal analysis identifies two spatial patterns of tumor and immune cell interdependence in DMG

To characterize the cellular composition of DMG within its spatial context, we employed a comprehensive multi-omics approach encompassing single-nuclei RNA sequencing (snRNA-seq), coarse (Visium) and single-cell resolution (CosMx) spatial transcriptomics (ST), and high-dimensional immunofluorescence (IF) imaging. We integrated data from public[21–24] and newly profiled samples, analyzing a total of 44 patients with DMG across modalities (Figure 1A; Table S1). After quality control of snRNA-seq data, we recovered 146,567 nuclei (Figure 1A). Malignant cell populations were identified based on the presence of inferred copy number variation (iCNV) (Figures S1A and S1B). In the malignant cell compartment, we identified principal cancer cell states previously described for DMG, encompassing AC-like, OPC-like, OC-like, and MES-like cells[7] (Figures 1B and S1C). Furthermore, consistent with previous findings,[7,18,19] the immune compartment was dominated by myeloid cells, with fewer tumor-infiltrating lymphocytes (TILs), including T and occasional B cells (Figures 1B and S1D). To assess the spatial co-occurrence of these immune and cancer cell subsets, we first analyzed 16 Visium samples (*n* = 51,124 spots; Figure 1A; Table S1), which revealed three distinct tumor-immune niches (Figures 1C and 1D; S2A and S2B). Regions enriched for the malignant MES program were characterized by infiltration of blood-derived immune cells, including monocyte-derived macrophages (MDMs) and TILs (collectively termed MES-niche; Figures 1C and 1D), consistent with patterns observed in adult GB.[25,26] Similar to GB,[27,28] these regions showed strong enrichment of hypoxia and pro-inflammatory mediators such as IFNγ, IFNα, and TNFα pathways, supporting active immune cell recruitment and potential activation (Figure 1F; Table S2). However, in line with hypoxia linked to immune suppression and T cell exhaustion in cancer,[29] including high-grade glioma,[30] we also detected anti-inflammatory signatures next to inflammatory responses. Thus, MES regions are shaped by a balance in immune activation and suppression, likely fostering immune cell recruitment while limiting effective T cell function. Whole-mount 3D imaging confirmed that, when recruited, T cells can remain tightly clustered within localized hotspots (Figure S2C), consistent with recent histological reports of rare inflammatory niches in DMG.[28] These hotspots showed minimal dispersal into the surrounding tissue, supporting the idea that active mechanisms restrict T cell infiltration into the tumor mass. The remainder of the tumor, representing ~60% of the spatially mapped regions, corresponded to niches enriched in developmental-like programs (AC-, OPC-, and OC-like), organized into two intermingled patterns collectively referred to as the AOO-niche (Figures 1C–1E). In contrast to MES-niches, these regions were enriched in microglia, showed a marked absence of MDMs, and contained fewer T cells. Using the single-cell resolution of the CosMx dataset (10 DMG cases; 23 patient samples, *n* = 26,552 cells) (Table S1), we confirmed the selective enrichment of MDMs within MES regions, while further resolving that microglia predominantly associate with AOO-like regions dominated by AC-like cells (Figure 1G). Although Visium data highlighted blood-derived immune infiltration within the MES regions, higher resolution analysis revealed an additional pattern characterized by TILs together with MDMs and microglia closely associated with blood vessels (pattern 0, Figures 1G–1I; S2D and S2E). In summary, we identify three spatially distinct tumor-immune ecosystems in DMG. MES regions show an enrichment of blood-derived MDMs, along with discrete areas that reflect localized immune-vascular interactions. In contrast, the dominant neurodevelopmental-like regions (AOO) are enriched in resident microglia and show minimal infiltration of blood-derived immune cells.

Microglia located within AOO-regions resemble homeostatic microglia and exhibit features in line with minimal blood-derived immune infiltration

Given the distinct distribution of microglia between AOO- and MES- regions, and differential intermingling with blood-derived immune cells, we sought to investigate the cellular and molecular differences between these spatially separated populations. Using the snRNA-seq dataset, we identified two distinct microglial subpopulations (Figures 2A and 2B). We next examined their spatial distribution and observed that microglia expressing inflammatory cytokines and chemokines involved in lymphocyte and monocyte recruitment (e.g., *IL1B*, *CCL3*, *CCL4*), overlapping with the recently described inflammatory microglia program,[32]

(G) Dot plot representation of cell-type enrichment within distinct spatial niches in DMG CosMx ST samples (*n* = 23).

(H) Representative FOVs illustrating identified spatial tumor-immune niches in CosMx datasets. Cells are segmented and colored according to the predicted cell subtype, and enriched cell types for each niche are annotated.

(I) Stacked barplot depicts the relative contribution of spatial patterns identified across CosMx ST samples (*n* = 23).

Please cite this article in press as: Collot et al., IGSF11-VISTA is a critical and targetable immune checkpoint axis in diffuse midline glioma, Cancer Cell (2025), https://doi.org/10.1016/j.ccell.2025.12.020

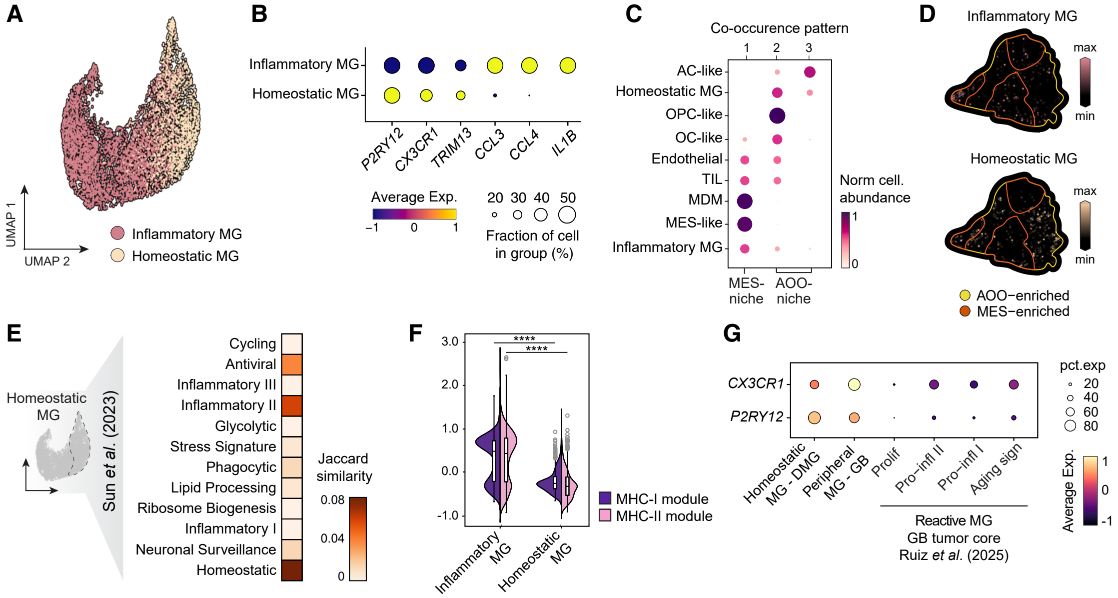

Figure 2. Homeostatic microglia spatially associate with the AOO-niche

(A) UMAP representation of microglia sub-populations in snRNA-seq data from patients with DMG ($n = 25$).

(B) Dot plot representation of the average expression of key microglial markers (color intensity) across microglia subpopulations ($n = 25$). Dot size indicates the percentage of cells expressing the marker within a certain population.

(C) Dot plot of tumor and immune cell co-occurrence patterns in Visium ST datasets ($n = 16$). Dot plots reflect estimated relative NMF weights normalized across components on a color and size scale.

(D) Spatial maps of compartment enrichment (color intensity) for homeostatic and inflammatory microglia. Line represents the AOO- (yellow) and MES-enriched (orange) areas.

(E) Jaccard similarity score (color intensity) for homeostatic microglia in DMG patient samples ($n = 25$) compared to a human brain reference dataset.[31]

(F) Violin plot of MHC-I (purple) and MHC-II (pink) related gene signature expression across microglia sub-populations ($n = 25$). $^{****}p < 0.0001$, Mann-Whitney U test.

(G) Dot plot shows the average expression (color intensity) of *P2RY12* and *CX3CR1* in DMG homeostatic microglia ($n = 25$) and in glioblastoma (GB) peripheral- and tumor core-associated microglia subsets from Ruiz-Moreno et al.[26] ($n = 109$). Dot size indicates the proportion of cells expressing each marker.

were enriched in MES-dominant regions (Figures 2C and 2D). Microglia in the AOO region showed high expression of homeostatic markers (*P2RY12* and *CX3CR1*) (Figures 2B–2D), recently reported to be enriched in K27M high-grade gliomas compared to pediatric low-grade gliomas,[20] and we show most closely resemble homeostatic microglia described in healthy brain[31] (Figure 2E; Table S2). In contrast to inflammatory microglia identified in MES regions, homeostatic-like microglia exhibited significantly lower expression of MHC-I and MHC-II gene signatures (Figure 2F; Table S2), a trait of brain-resident microglia under homeostatic conditions and indicative of reduced antigen presentation.[33] A lack in gene expression encoding for chemokines and inflammatory proteins in homeostatic-like microglia (Figure S3A) further confirms their homeostatic-like state, in line with the poor blood-derived immune cell recruitment in AOO-enriched regions. Interestingly, this microglial compartment (*P2RY12* and *CX3CR1*-positive) differs from what we previously observed in adult high-grade gliomas.[26] In GB, homeostatic microglia are restricted to the tumor periphery,[26] while the majority of intratumoral microglia reflect inflammatory states (Figure 2G). This reveals spatially restricted microglia populations in DMG, characterized by a dominant homeostatic-like phenotype associated with the AOO region and absent in the GB tumor core.

Enrichment of the IGSF11-VISTA pathway in AOO regions

Given the unique, DMG-specific immune landscape, especially in the AOO niches, we inferred ligand-receptor (L-R) interactions from snRNA-seq data to explore immune-cancer communication. This identified five global communication patterns across cells and signaling pathways, with microglia emerging as the main sender of pattern 2 (Figures S3B and S3C). The L-R pairs driving this pattern are typically involved in immune activity and regulation, including several immune checkpoints, such as TIM-3 and GALECTIN (Figure S3C). This pattern also revealed an underappreciated immune checkpoint (IC) pathway, the V-domain immunoglobulin suppressor of T cell activation (VISTA/VSIR), together with its ligand immunoglobulin superfamily member 11 (IGSF11/VSIG3)[34,35] (Figures S3C and S3D; Table S3). VISTA is a negative checkpoint regulator that inhibits T cell activation early in the cascade.[36] Beyond T cells, it also regulates multiple myeloid-cell functions, including apoptotic cell clearance.[37,38] Interestingly, IGSF11-VISTA signaling was predicted to be strongest between AOO-like tumor cells and microglia (Figure 3A). Using a complementary tool for the analysis of spatial communication (COMMOT), we confirmed a strong spatial interaction between *VSIR* and *IGSF11*, along with higher expression within the AOO region in the Visium samples (Figures 3B and 3C). *VSIR* was

Please cite this article in press as: Collot et al., IGSF11-VISTA is a critical and targetable immune checkpoint axis in diffuse midline glioma, Cancer Cell (2025), https://doi.org/10.1016/j.ccell.2025.12.020

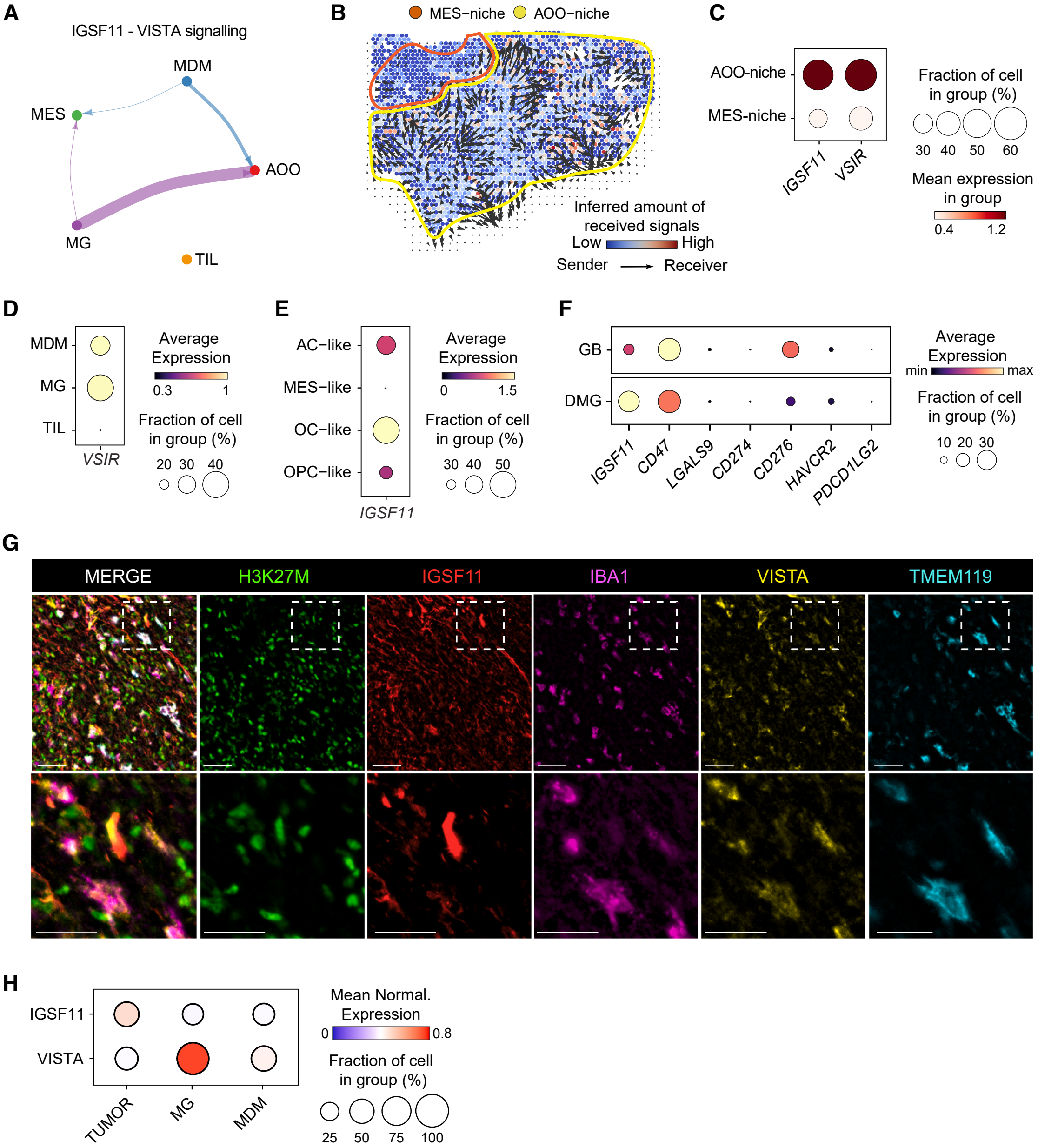

Figure 3. Ligand-receptor interaction analysis identifies IGSF11-VISTA as an immune checkpoint axis enriched in the AOO niche

(A) Circos plot depicts the predicted interactions mediated by the IGSF11–VISTA pathway across selected tumor and immune compartments. Arrows indicate the direction of signaling, and the thickness of edges corresponds to interaction probability.

(B) Signaling direction of the VISTA signaling pathway in a human DMG sample profiled by Visium ST, colored by the inferred amount of received signals computed by COMMOT. Line represents the AOO- (yellow) and MES-enriched (orange) areas.

(C) Dot plot visualization of *IGSF11* and *VSIR* expression (color intensity) across Visium spatial niches ($n = 16$). Dot size represents the percentage of spatial spots expressing the marker.

(D and E) Relative expression (color intensity) of *VSIR* across immune (D) and *IGSF11* across DMG tumor populations (E) ($n = 25$). Datapoint size indicates the percentage of expressing cells.

(F) Dot plot visualization of relative immune checkpoint expression (color intensity) within human DMG ($n = 25$) or GB ($n = 109$) tumor cells. Dot size indicates the percentage of cells expressing the marker.

(G) 2D overview image (top) and zoom in (bottom) of DMG autopsy tissue stained for H3K27M (green), IGSF11 (red), IBA1 (magenta), VISTA (yellow), and TMEM119 (cyan). Dashed square indicates the area depicted in the zoom. Scale bars, 50µm (overview) and 10µm (zoom).

(H) Dot plot visualization of the mean normalized expression (color intensity) for IGSF11 or VISTA in selected cells of human DMG tumors ($n = 4$). Dot size indicates the percentage of cells expressing the marker.

Please cite this article in press as: Collot et al., IGSF11-VISTA is a critical and targetable immune checkpoint axis in diffuse midline glioma, Cancer Cell (2025), https://doi.org/10.1016/j.ccell.2025.12.020

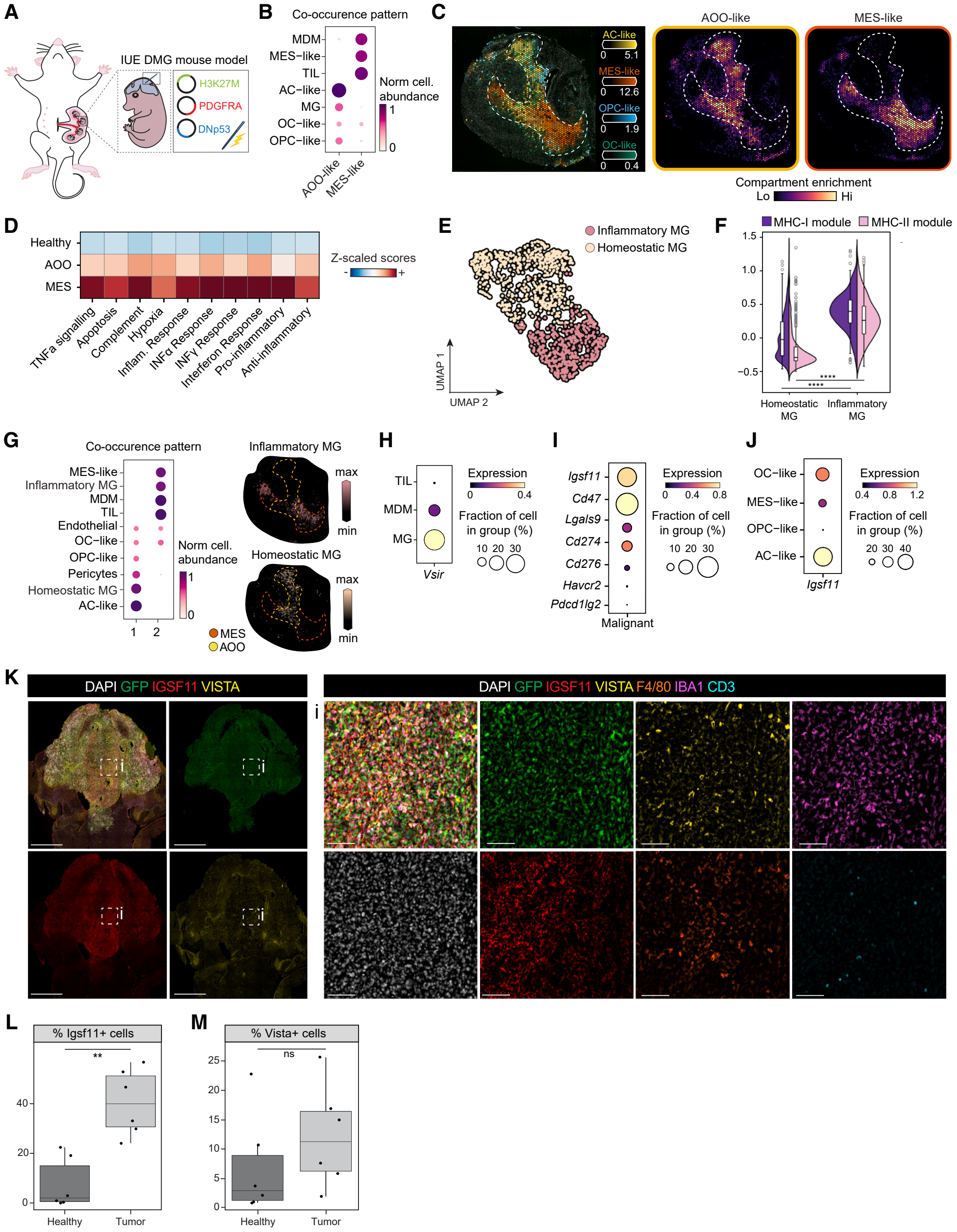

Figure 4. DMG tumor-immune spatial organization and the IGSF11-VISTA pathway are preserved in mice

(A) Schematic representation of the *in-utero* electroporation (IUE) mouse model dependent on DMG driver mutations.

(B) Dot plot representation of the co-occurrence patterns in Visium ST data ($n = 4$). Dot plots reflect estimated relative NMF weights normalized across components on a color and size scale.

(C) Visium ST data depicting estimation of DMG cancer cell states abundance (color intensity) overlayed on top of the tissue image (left). Spatial representation of the co-occurrence patterns, shown as compartment enrichment (color intensity) with a dashed line delineating the tumor border (right).

(D) Heatmap visualization of z-scaled expression scores (blue-to-red color gradient) for biological and immune processes across mouse healthy brain and AOO- and MES-enriched tumor areas ($n = 4$).

(E) UMAP representation of mouse microglia sub-populations ($n = 4$).

(legend continued on next page)

predominantly expressed by microglia, consistent with expression patterns in the healthy brain.[39] MDMs also expressed *VSIR*, reflecting its known broader hematopoietic distribution,[38] particularly in myeloid cells (Figure 3D). *IGSF11* was predominantly expressed in OC-, AC-, and OPC-like cancer states (Figure 3E). When comparing the expression of *IGSF11* across prominent ICs, such as *CD274* (PD-L1), *PDCD1LG2* (PD-L2/CD273) and *CD276* (B7-H3), *IGSF11* was most highly expressed in DMG patient samples as opposed to adult GB (Figure 3F), even surpassing the expression of *CD47*, encoding a protein that inhibits macrophage-mediated phagocytosis and that has been suggested as a promising target in various cancers, including DMG.[40] Protein-level validation confirmed IGSF11 expression on tumor cells and VISTA on both microglia and to a lesser extend MDMs (Figures 3G and 3H). Analysis of publicly available gene expression datasets on the R2 Platform confirmed robust expression of *IGSF11* and *VSIR* in DMG tumor samples (45 samples) and overall pediatric gliomas (330 and 212 samples for high- and low-grade glioma, respectively). Especially *IGSF11*, surpassed expression levels observed in other pediatric central nervous system tumors (Figure S3E). Thus, *VSIR* expression by myeloid cells, and in particular microglia, together with its ligand *IGSF11,* predominantly associating with the AOO tumor niche, highlights this pathway as a potential therapeutic target in DMG and potentially other pediatric gliomas.

IGSF11-VISTA represents a preserved mechanism that can be modeled in immune-competent mice

To analyze the impact of IGSF11 on tumor-immune interaction, we first turned to an immune-competent DMG mouse model depending on *in utero* electroporation (IUE) of H3.3K27M and accompanying mutations DNp53 and PDGFRA[41–43] (Figure 4A). Malignant cells in this model can be identified based on plasmid reporter *eGFP* (*H3K27M-eGFP*) expression in snRNA-seq (Figure S4A) and ST (Figure S4B) data. Importantly, *de novo* DMG in this IUE model shows a high similarity score with primary DMG patient material, as opposed to cell lines and patient-derived xenografts (PDXs)[6] (Figure S4C), demonstrating the suitability of this model for studying the heterogeneous DMG cellular landscape in an immune-intact *in vivo* environment. Accordingly, snRNA-seq analysis identified AC-, OPC-, OC-, and MES-like cells within the tumor eGFP$^+$ population (Figure S4A, D). The immune compartment contained few T and B cells, whereas myeloid cells were found in abundance, consistent with patient samples. Because the murine model allows for larger sampling, we could also identify in the myeloid compartment, besides microglia and MDMs, a lower abundance population of border-associated macrophages (BAMs) (Figure S4E). Moreover, similar to patient data, spatial analysis demonstrated segregation into developmental AOO-enriched areas, containing microglia, but devoid of infiltrating immune cells and MES regions associating with MDMs and T cells (Figures 4B and 4C). As observed in human samples, MES regions displayed elevated pro-inflammatory signaling, including IFNγ, IFNα, and TNFα, together with hypoxia, apoptosis, and anti-inflammatory gene expression, suggesting a balance that recruits immune cells but limits effective T cell function (Figure 4D). Rare, spatially restricted immune hotspots were also observed, typically one to two per tumor (Figure S4F). Also in mice, microglia could be further segregated into inflammatory microglia and a homeostatic population (Figure 4E and S4G). The murine inflammatory and homeostatic microglia populations showed a strong resemblance to these subsets in our patient data cohort (Figure S4H), and again, homeostatic microglia displayed reduced MHC-I/-II gene expression (Figure 4F) and were spatially associated with the AOO-enriched regions (Figure 4G). Together, this shows that the IUE model recapitulates spatially organized tumor and microglia cell states observed in patients. Moreover, unbiased cluster analysis of L-R data from both human and murine samples revealed five preserved signaling pathway clusters, including a VISTA-containing cluster that exhibits a high degree of functional similarity, with main sending and receiving cell types conserved between the human and mouse datasets (Figure S4I). Consistent with human tumors, *Vsir* expression was higher in microglia (Figure 4H), while its ligand *Igsf11* ranked among the top immune checkpoints (Figure 4I) and was most highly expressed in AC- and OC-like tumor cells (Figure 4J). Immunofluorescence analysis confirmed Vista protein expression in microglia and strong Igsf11 expression within the tumor region compared to surrounding healthy tissue, supporting its potential as an effective on-target, on-tumor therapeutic axis, where tumor-specific overexpression is essential (Figures 4K–M and S4J). Thus, data from the IUE mouse model confirm its faithfulness to patient samples, particularly in spatial organization, providing a relevant system to experimentally test the impact of IGSF11-VISTA signaling on DMG tumors.

Loss of *Igsf11* leads to DMG tumor reduction and survival

Given its predominant expression in cancer cells, in contrast to VISTA's broader distribution and pleiotropic immune functions[39] (Figure 4M), IGSF11 may represent a more tumor-restricted

(F) Violin plot of MHC-I (purple) and MHC-II (pink) related gene signature expression across microglia sub-populations ($n = 4$). $^{****}p < 0.0001$, Mann-Whitney U test.

(G) Dot plot (left) of tumor and immune cell co-occurrence patterns in ST datasets, segregating between homeostatic and inflammatory microglia ($n = 4$). Dot plots reflect estimated relative NMF weights normalized across components on a color and size scale. Spatial maps (right) of compartment enrichment (color intensity) for homeostatic and inflammatory microglia. Dashed line represents the AOO- (yellow) and MES-enriched (orange) areas.

(H) Relative expression (color intensity) of *Vsir* across immune populations ($n = 4$). Datapoint size indicates the percentage of expressing cells.

(I) Relative expression (color intensity) of immune checkpoints in mouse DMG tumor cells ($n = 4$). Datapoint size indicates the percentage of expressing cells.

(J) Relative expression (color intensity) of *Igsf11* across mouse DMG tumor populations ($n = 4$). Datapoint size indicates the percentage of expressing cells.

(K) 2D overview image (left) and zoom in (right) on the area outlined by a dashed square (i) of a mouse DMG tumor-bearing brain. Tissue slice stained for DAPI (gray), tumor-eGFP (green), IGSF11 (red), IBA1 (magenta), VISTA (yellow), F4/80 (orange), and CD3 (cyan). Scale bars, 1mm (overview - left) and 50μm (zoom - right).

(L and M) Frequency of Igsf11$^+$ (L) or Vista$^+$ (M) cells in the tumor compared to the healthy brain region ($n = 6$). Boxplots show the interquartile range with the median indicated, and whiskers represent 1.5x the interquartile range. $^{**}p < 0.01$, Wilcoxon test, ns = not significant.

Please cite this article in press as: Collot et al., IGSF11-VISTA is a critical and targetable immune checkpoint axis in diffuse midline glioma, Cancer Cell (2025), https://doi.org/10.1016/j.ccell.2025.12.020

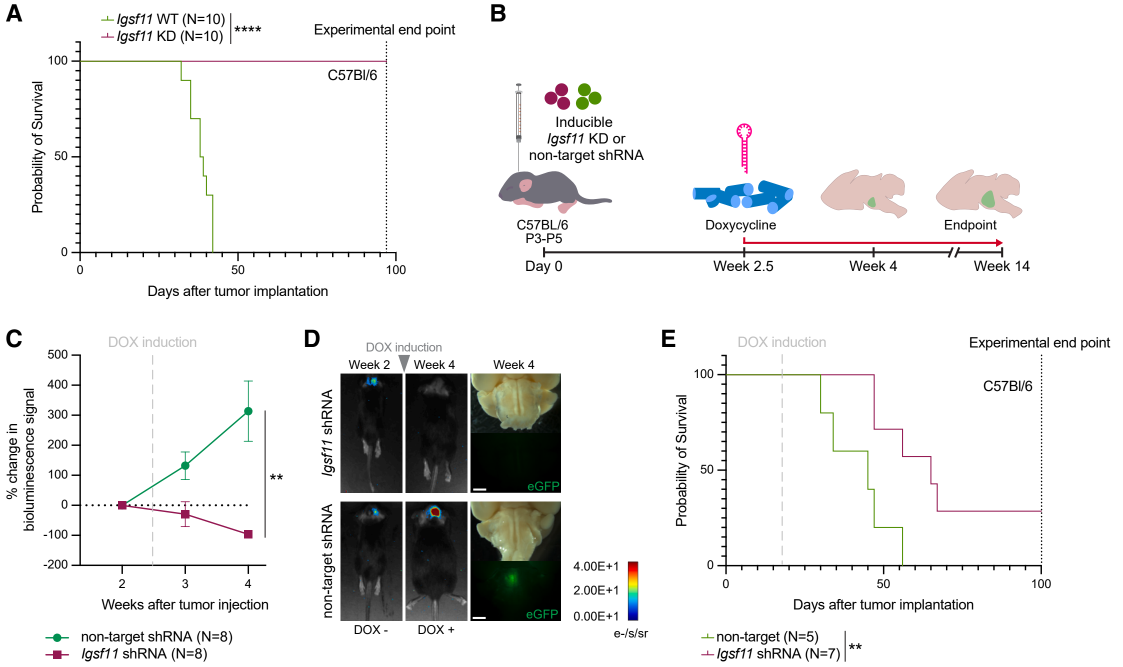

Figure 5. *In vivo* inducible *Igsf11* knockdown demonstrates the therapeutic potential of IGSF11 targeting

(A) Kaplan-Meier survival curves of immunocompetent C57Bl/6 mice allografted with WT (n = 10) or *Igsf11* KD cells (n = 10). ****p=<0.0001, Log rank Mantel-Cox test.

(B) Schematic representation of doxycycline (DOX)-dependent induction of *Igsf11* or non-target shRNA in 24B7 cells injected into C57BL/6 pups. Continuous induction of the construct was initiated from 2.5 weeks post-tumor cell injection by providing DOX-containing food pellets (red line).

(C) Longitudinal assessment of tumor burden by bioluminescence imaging (BLI) following the injection of 24B7 cells (inducible *Igsf11* shRNA or non-target shRNA, n = 8) into C57BL/6 mice. Line plot (mean ± SEM) showing changes in BLI signal relative to baseline (2 weeks post-injection). The dashed line marks the start of DOX-dependent construct activation. **p=<0.01, t test.

(D) Representative BLI images at 2 weeks (DOX-) and 4 weeks (DOX+) post-injection (left), and overview of tumor burden by imaging (eGFP) in the pontine brain region at 4 weeks post-injection and 10 days after construct induction (right). Scale bars, 2 mm.

(E) Kaplan-Meier survival curves of immunocompetent mice injected with inducible *Igsf11* shRNA (n = 7) or non-target shRNA (n = 5) 24B7 cells. Dashed line (gray) indicates the start of DOX-dependent construct induction. **p=<0.01, Log rank Mantel-Cox test.

target with a lower risk of systemic immune dysregulation. It also offers a means to preferentially target the AOO niche, the developmental-like DMG compartment, whereas the MES program has been more extensively explored therapeutically in glioma and other cancers.[44] Furthermore, *IGSF11* has been linked to tumor progression and poor prognosis,[45,46] but its direct functional role in tumor-immune interactions remains unexplored. To address this, we used our IUE mouse model to conduct a loss-of-function study using an shRNA-based knockdown (KD) approach targeting *Igsf11* (Figure S5A). Bioluminescence imaging (BLI) to assess tumor burden revealed a gradual reduction in signal intensity over time in the *Igsf11* KD IUE tumors compared to *Igsf11* wild-type (WT) controls (Figure S5B). Using immunofluorescence imaging, we compared the microenvironment of *Igsf11* WT and KD tumors with that of a healthy control brain. In both tumor conditions, the tumor bed was distinctly delineated by pronounced Gfap and Iba1 expression, indicative of reactive astrocytes and myeloid cells, respectively[47,48] (Figure S5A). However, in line with the BLI data, the *Igsf11* KD tumor bed exhibited significantly fewer tumor cells, providing evidence of partial tumor clearance. Interestingly, in the *Igsf11* KD model, very few T cells were observed at the tumor site after clearance (Figures S5A and S5C). Together, these data suggest a role for Igsf11 in regulating DMG clearance, which may not be mediated by cytotoxic T cells. To investigate its targeting potential further, we employed a syngeneic mouse model that offers higher tumor penetrance and throughput.[49] This model uses a DMG spheroid cell line derived from the IUE model, in which we confirmed Igsf11 expression in WT cells, whereas engineered KD cells showed a marked decrease (Figure S5D). We transplanted these WT and KD DMG cells into immunocompetent mice, revealing a significant survival benefit of mice transplanted with *Igsf11* KD cells (Figure 5A). 100% of the *Igsf11* KD cohort reached the experimental endpoint without physiological signs of tumor burden, while all mice receiving WT DMG cells had to be sacrificed due to weight loss or other brain malignancy-related symptoms. Notably, the average survival span of mice bearing WT DMG was 38 days. Thus, cut short by the experimental endpoint of our study, *Igsf11* KD tumors offered a vast survival benefit that is expected to extend beyond the current 97-day cut-off timepoint.

Therapeutic impact of IGSF11-VISTA targeting

Encouraged by the outcomes of *Igsf11* KD, we sought to validate the impact of *Igsf11* modulation as a treatment strategy. We first used an inducible *Igsf11* KD system to trigger gene silencing in

Please cite this article in press as: Collot et al., IGSF11-VISTA is a critical and targetable immune checkpoint axis in diffuse midline glioma, Cancer Cell (2025), https://doi.org/10.1016/j.ccell.2025.12.020

established tumors. We used DMG cells engineered to express an *Igsf11* or non-target shRNA under control of the TET-On 3G promoter, and induced *Igsf11* deletion 2 weeks after tumor engraftment through doxycycline provided in the food (Figure 5B and S5E). BLI imaging and 3D imaging of $eGFP^+$ tumors showed comparable tumor growth rates prior to the deletion of *Igsf11* but significantly reduced tumor burden upon deletion (Figures 5C and 5D). In line with this, we observed a significant survival benefit compared to the non-target shRNA group, with 2/7 mice from the inducible *Igsf11* KD group still alive at the day 100 experimental endpoint without clinical signs of disease (Figures 5E and S5F). The lack of 100% survival in this setting likely reflects reduced penetrance of the inducible system, as at 4 weeks post-treatment, the few remaining tumor cells still exhibited Igsf11 expression (Figures S5G and S5H). Nevertheless, it also demonstrates the potential of *Igsf11* targeting in a therapeutic setting by controlling tumor progression rather than initiation. To further support a therapeutic application, we used a blocking antibody rather than genetic IGSF11 modulation. First, we treated tumor-bearing brain slices from IUE mice with a VISTA-blocking antibody[50] (anti-VISTA, SG7). After 5 days of treatment, a significant decrease in tumor size could be seen compared to the isotype control (Figure S5I). A similar VISTA-blocking approach using DMG patient samples,[51] also demonstrated tumor control (Figure S5J) with a significant reduction in the percentage of $H3K27M^+$ tumor cells upon treatment *ex vivo* (Figure S5K). This positive impact of Igsf11 signaling inhibition through a blocking antibody in murine and patient samples further supports IGSF11-VISTA targeting as a therapeutic option for DMG.

Tumor clearance in the absence of Igsf11 is microglia-dependent

Having demonstrated the therapeutic potential of IGFS11-VISTA targeting, we sought to explore the underlying mechanisms driving its effect on tumor control. Given microglia as the primary receiver of IGSF11 signaling (Figure 3A) and no signs of T cell involvement in IUE *Igsf11* KD experiments (Figures S5A and S5C), we first aimed to establish a local brain-intrinsic immune control mechanism by repeating *Igsf11* KD in severely immunocompromised NSG mice, lacking T, B, and NK cells and displaying reduced macrophage recruitment.[52,53] Also in this immunocompromised setting, 100% of the *Igsf11* KD cohort reached the experimental endpoint (100 days), whereas *Igsf11* WT tumor-bearing mice had an average survival of 35 days (Figure 6A). These findings strongly suggest that brain-resident microglia play a critical role in recognizing and clearing *Igsf11* KD tumor cells. This was further supported by immunofluorescence imaging in immunocompetent mice with *Igsf11* WT and KD tumor cells. Consistent with previous findings in the IUE model, the presence of $CD3^+$ T cells in the TME of *Igsf11* KD tumors was minimal (Figures 6B and 6C), similar to control tumors. Both conditions exhibited a dense association of microglia with tumor cells, with only a sparse presence of MDMs ($Iba1^+$, $Itga4/Cd49d^+$)[54]; however, *Igsf11* KD tumors displayed significantly elevated levels of cleaved caspase-3 (cCASP3) in these areas (Figures 6B and D). This increase in apoptosis coincided with enhanced presence of microglia exhibiting signs of phagocytic activity (Figures S6A–S6C). Furthermore, additional quantification of immune populations in the inducible *Igsf11* KD, using the residual tumoral tissue two weeks post-induction, showed no significant increase in T cell or MDM infiltration (Figure S6D). Interestingly, *Igsf11* KD did not lead to an increase in antigen-presenting microglia ($MHC\text{-}II^+$) (Figure S6E), which may explain the absence of blood-derived immune cell recruitment. Collectively, these findings indicate that the observed survival benefit is not primarily driven by recruited immune cells but rather by active targeting of *Igsf11* KD tumor cells by brain-resident microglia. To unambiguously demonstrate an active role of microglia in tumor control, we depleted NSG mice of microglia by treating them with the Csf1r inhibitor PLX3397 in the food prior to tumor implantation (Figure 6E). Microglia depletion was confirmed by 3D imaging (Figure S6F) and quantification of Iba1 expressing cells (Figure S6G). Quantification of the tumor area 20 days post injection revealed that in the absence of microglia, tumors derived from *Igsf11* KD cells progressed similarly to WT tumors (Figure 6F). A comparable outcome was observed in immune-competent mice depleted of microglia (Figure S6H), demonstrating that T cells and macrophages do not perform tumor control in the absence of microglia. Thus, the therapeutic effect of *Igsf11* deletion in DMG tumors is dependent on the presence of functional microglia.

To validate this in a human context, we employed a recently developed human brainstem organoid model, which we showed faithfully recapitulates the neuronal and glial microenvironment of DMG.[55] Incorporation of primitive macrophage progenitors (PMPs) into this system resulted in robust microglial differentiation with upregulated *VSIR* expression (Figure S6I). Co-culture with either *IGSF11* WT or KO patient-derived DMG cells[24] (Figure S6J) revealed a significant reduction in *IGSF11* KO GFP^+ tumor cells compared to WT (Figures 6G and 6H). In addition, *IGSF11* KO cells exhibited apoptotic features, demonstrated by positive cCASP3 staining (Figure S6K). Importantly, these effects were only observed in the presence of microglia. When brainstem organoids without integrated microglia were used, tumor cell presence was similar (Figures 6G and 6H), and no upregulation of cCASP3 was observed (Figure S6K). These results demonstrate that in a human setting, microglia are also essential for controlling DMG in the absence of IGSF11 signaling.

Igsf11 reinforces microglia Vista expression and regulates their homeostatic state

To investigate how Igsf11 signaling regulates microglia *in vivo*, we implemented a complementary overexpression (OE) approach (*Igsf11* OE). Overexpression relative to WT and *Igsf11* KD tumor cells was confirmed by qPCR (Figure S7A). *In vitro* comparison showed that *Igsf11* OE significantly increased proliferation and metabolic activity relative to WT and KD tumor cells (Figure S7B-C), indicating that Igsf11 promotes intrinsic tumor growth capacity when levels exceed physiological Igsf11 expression. We transplanted *Igsf11*-OE DMG tumor cells into immunocompetent mice to assess changes in tumor-immune interactions. As expected from the *in vitro* data, endpoint quantification revealed increased *Igsf11* OE tumor burden compared to WT tumors (Figure 7A). Despite their larger size, *Igsf11* OE tumors were associated with prolonged survival (median survival = 65 days) relative to WT tumors (36 days),

Please cite this article in press as: Collot et al., IGSF11-VISTA is a critical and targetable immune checkpoint axis in diffuse midline glioma, Cancer Cell (2025), https://doi.org/10.1016/j.ccell.2025.12.020

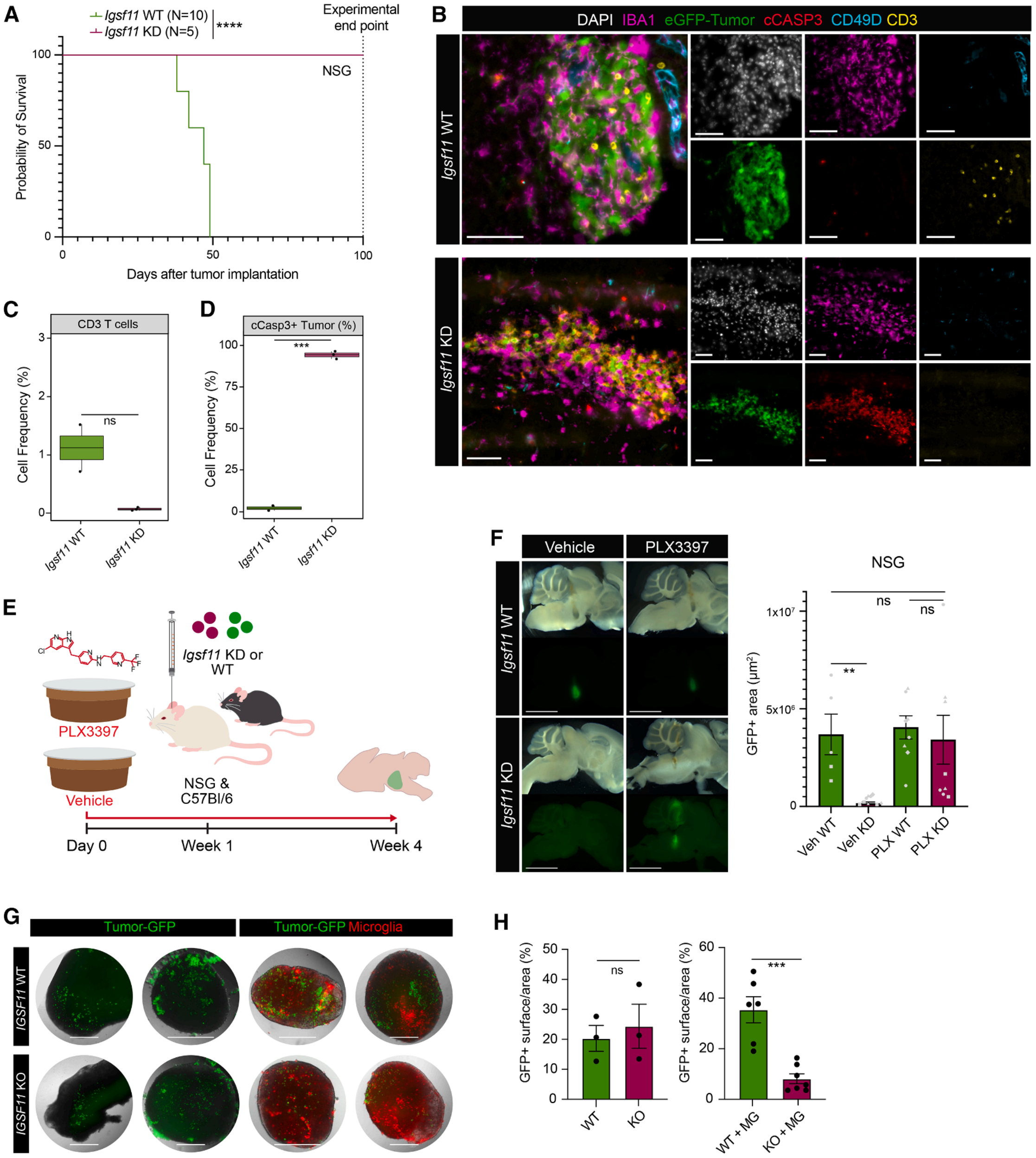

Figure 6. Microglia are indispensable for tumor clearance in the absence of Igsf11

(A) Kaplan-Meier survival curves of immunocompromised NSG mice allografted with WT (*n* = 5) or *Igsf11* KD cells (*n* = 10). ****$p < 0.0001$, Log rank Mantel-Cox test.

(B) 2D images of *Igsf11* KD or WT tumor beds, 4 days after implantation. Stained for DAPI (gray), tumor-eGFP (green), IBA1 (magenta), CD3 (yellow), CD49D (cyan), and cCASP3 (red). Scale bars, 50 µm.

(C and D) Cell frequency of $CD3^+$ T cell numbers (C) and $cCASP3^+$ tumor cells (D) in *Igsf11* WT (*n* = 2) and *Igsf11* KD (*n* = 3) murine DMG tumors, 4 days after implantation. Boxplots show the interquartile range with the median indicated, and whiskers represent 1.5x the interquartile range. ***$p < 0.001$, *t* test. ns = not significant.

(E) Schematic representation of microglia depletion schedule using PLX3397 (or vehicle) in food, implantation of *Igsf11* WT or KD 24B7 tumor cells, and harvest time point.

(F) Representative stereo images (left) of the tumor burden (eGFP signal – green) in NSG mouse brain sections treated with PLX3397 (PLX) or vehicle control and receiving Igsf*11* WT or KD 24B7 tumor cells. Scale bars, 5mm. Bar plot (right) displaying tumor area quantification for (n = 1–3) brain sections from (n = 2–4) mice per treatment condition. Symbols refer to individual mice. Bar graphs indicate the mean ± SEM. **$p < 0.01$, Dunn's multiple comparisons, ns = not significant.

(G) Representative images of brainstem organoid slices with or without integrated microglia (red) co-cultured with *IGSF11* WT or KO BT093 DMG cells (GFP, green). Scale bars, 500µm.

(H) Percentage of GFP+ surface per brainstem organoid slice with (n = 6–7) or without microglia (*n* = 3) upon co-culture with *IGSF11* WT or KO BT093 DMG cells. Bar graphs indicate the mean ± SEM. ***$p < 0.001$, *t* test.

Please cite this article in press as: Collot et al., IGSF11-VISTA is a critical and targetable immune checkpoint axis in diffuse midline glioma, Cancer Cell (2025), https://doi.org/10.1016/j.ccell.2025.12.020

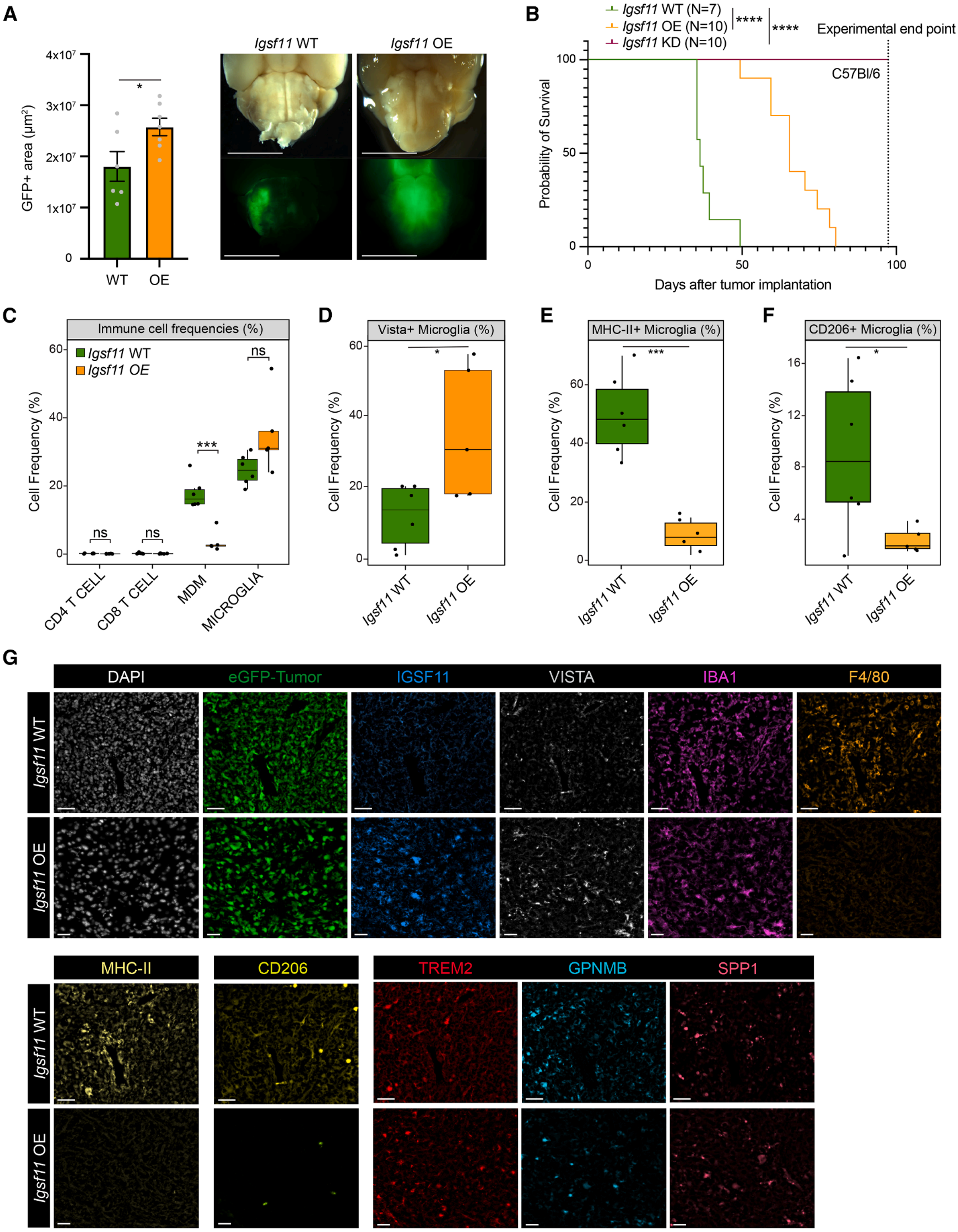

Figure 7. Igsf11 signaling reinforces VISTA expression and maintains microglia in a homeostatic state

(A) Quantification of survival study endpoint eGFP+ tumor area (left) in the pons of mice receiving *Igsf11* WT ($n = 6$) or OE ($n = 7$) tumor cells. Bar graphs indicate the mean ± SEM. $*p < 0.05$, *t* test. Representative stereo images (right) of the tumor signal (green) in the pontine region. Scale bars, 5mm.

(B) Kaplan-Meier survival curves of immunocompetent C57Bl/6 mice allografted with WT ($n = 7$), KD ($n = 10$), or *Igsf11* OE tumor cells ($n = 10$). $****p < 0.0001$, Log rank Mantel-Cox test.

(C) Immune cell frequencies in *Igsf11* WT (green) and *Igsf11* OE (orange) DMG tumors (n = 5–6). Boxplots show the interquartile range with the median indicated, and whiskers represent 1.5x the interquartile range. $***p < 0.001$, *t* test.

(legend continued on next page)

Please cite this article in press as: Collot et al., IGSF11-VISTA is a critical and targetable immune checkpoint axis in diffuse midline glioma, Cancer Cell (2025), https://doi.org/10.1016/j.ccell.2025.12.020

although not to the same extent as in *Igsf11* KD tumor recipients (Figure 7B). To understand this seemingly contradictory prolonged survival in the face of enhanced tumor growth, we applied cyclic immunofluorescence (cIF) imaging to characterize the tumor-immune microenvironment. We used a panel of 16 antibodies to profile tumor and immune cells across WT and *Igsf11* OE cohorts (Figures S7D and S7E). In total, over 1,1 million cells were annotated into 10 subtypes, spanning lymphoid, myeloid, healthy, and tumor populations (Figure S7D). CD4 and CD8 T cells remained scarce in both WT and *Igsf11* OE tumors, representing ∼1% of immune cells. In contrast, MDMs (Iba1$^+$/F4/80$^+$) were significantly reduced in *Igsf11* OE tumors (Figure 7C). These tumors also showed a trend toward increased microglia at the tumor site and a significantly higher fraction of Vista-expressing microglia (Figures 7C and 7D), suggesting that tumor-derived Igsf11 induces the expression of its receptor on microglia in a feedforward loop. Consequently, microglia became less immunostimulatory, reflected by a significant reduction in MHC-II expression, a hallmark of homeostatic microglia[56] (Figures 7E–7G and S7F and S7G). An accompanying decrease in CD206, a myeloid immunosuppressive marker (Figures 7F and 7G and S7E and S7F), further confirms this neutral state. We also examined Spp1, Gpnmb, and Trem2, essential for microglial function, but whose overexpression has been associated with primed or activated microglia in the healthy brain, and with disease-associated microglia in aging, neurodegenerative disorders, and glioma.[57,58] We did not observe a significant increase in these markers upon *Igsf11* overexpression (Figures 7G and S7F and S7G), further supporting the notion that microglia under Igsf11 signaling preserve a homeostatic phenotype. This non-inflamed state might also explain why, despite the accelerated progression of *Igsf11*-overexpressing tumors, mice survive longer (Figure 7B). Thus, IGSF11-VISTA signaling maintains microglia in a homeostatic state, evoking a brain-intrinsic non-inflammatory immune control mechanism when targeted that induces tumor elimination.

DISCUSSION

We profiled the spatial organization of H3K27M-altered DMG, uncovering a predominance of AOO-niches, which uniquely to DMG, as compared to adult GB, present with homeostatic-like microglia. VISTA was expressed by homeostatic microglia, whereas its ligand IGSF11,[45] was enriched in tumor cells in the AOO niches. We employed several complementary approaches to experimentally demonstrate that IGSF11-VISTA signaling represents a targetable immune checkpoint axis in DMG. *In vivo* inducible *Igsf11* KD demonstrated the effectiveness of IGFS11 targeting in established tumors, which was further confirmed by the efficacy of VISTA-blocking antibodies *ex vivo*, also on patient samples. We combined NSG mice lacking adaptive immunity[52,53] with microglia depletion using the CSF1R inhibitor PLX3397 to demonstrate that microglia are the primary mediators of tumor control in the absence of Igsf11. We were able to recapitulate this microglia-dependent tumor control mechanism in a fully human setting, using our most advanced human brainstem organoid model,[55] confirming that microglia alone are sufficient to restrain human DMG tumor cells in the absence of additional immune compartments. *Igsf11* overexpression in mice showed that tumor Igsf11-driven signaling promotes the homeostatic-like phenotype of microglia in a feedforward loop, enhancing the proportions of Vista$^+$ microglia. Altogether, these findings uncover a brain-intrinsic and potentially non-immunogenic tumor killing mechanism, as MCH-II expression on microglia remained low upon inducible *Igsf11* deletion, suggesting that their immune-activating properties are limited. Together with the lack of T cell recruitment, this potentially implies less risk for (adaptive) immune-induced toxicity.[59] In line with this, immunocompetent recipient mice of *Igsf11* KD tumor cells did not show signs of immune-related toxicity or symptoms and, instead, displayed 100% survival. A specific population of MDMs has been correlated to survival benefit in high-grade glioma patient data,[60] however, the prevailing view remains that tumor-associated macrophages, including both MDMs and microglia, predominantly exert pro-tumoral functions. Consequently, they have become the focus of therapeutic strategies aimed at either depleting them or limiting their tumor-supportive roles, or, as in our case, reprogramming them toward anti-tumor activity.[61–64] Our findings may help explain why CSF1R inhibitor-based depletion strategies have proven unsuccessful in targeting DMG[20] and GB,[65] as effective tumor control appears to depend on preserving and harnessing the anti-tumor functions of brain-resident microglia rather than broadly depleting or impairing both microglia and MDMs.

Our findings that IGSF11 maintains microglia in a homeostatic state matches with its unique expression profile at immune privileged sites that require immune homeostasis to prevent inflammatory tissue damage. Except for the brain and testis (IGSF11 is also known as brain- and testis-specific IgSF protein (BT-IgSF)),[66] IGSF11 is minimally detected in other tissues compared to other immune checkpoints.[46] Furthermore, we show that Igsf11 expression is higher in the tumor area than in surrounding healthy brain tissue, which was not the case for VISTA. While several VISTA antagonists are currently in clinical trials,[46] one trial was terminated due to cytokine release syndrome-related side effects.[67] Given its spatially restricted expression pattern, this highlights the potential advantage of targeting IGSF11 directly. However, the benefit in terms of reduced toxicity awaits confirmation using systemically administered blocking agents.

The 100% survival benefit reached in our *Igsf11* KD cohort exceeds what has been observed in other preclinical immunotherapy settings,[68] including GD2 CAR T cells,[69] which have now entered clinical trials for DMG.[70,71] However, in our experimental set-up, more representative of patient treatment schemes (inducible *Igsf11* KD), we achieved tumor eradication in all mice, yet 80% subsequently developed tumor recurrence. While this may in part reflect technical limitations, it also suggests that combinatorial strategies could provide additional

(D–F) Frequency of Vista$^+$ (D), MHCII$^+$ (E), or CD206$^+$ (F) microglia in *Igsf11* WT (green) and OE (orange) DMG tumors (n = 5–6). Boxplots show the interquartile range with the median indicated, and whiskers represent 1.5x the interquartile range. $^*p < 0.05$, $^{***}p < 0.001$, *t* test.

(G) 2D overview image of an *Igsf11* WT and OE tumor tissue slice stained for DAPI (gray), eGFP-Tumor (green), Igsf11 (blue), VISTA (white), IBA1 (magenta), F4/80 (orange), MHCII (yellow), TREM2 (red), CD206 (green), SPP1 (pink), and GPNMB (cyan). Scale bars, 50μm.

Please cite this article in press as: Collot et al., IGSF11-VISTA is a critical and targetable immune checkpoint axis in diffuse midline glioma, Cancer Cell (2025), https://doi.org/10.1016/j.ccell.2025.12.020

therapeutic benefit, particularly those targeting complementary mechanisms within the MES region.[72] While MES-like tumor cells have traditionally been prioritized in brain cancer research due to their aggressive nature and extensive immune interactions,[10,16,73,74] our target specific to the AOO-region, reaching such a profound outcome, highlights the importance of this developmental-like region for tumor progression. This is further supported by our data showing that AOO areas are more abundant, while MES-like regions are less frequent, in children compared to adults.[7] However, also in GB, where recent spatial profiling efforts revealed a similar segregation into MES-dominated versus AC- and OC-associated patterns,[28,75] the latter represented the most aggressive tumor area, where tumor cells showed the highest infiltrative behavior.[28] Together with our current findings, this warrants more research into the classically overlooked AOO tumor region across pediatric and adult brain oncology.

Recent work demonstrates that resident microglia are reduced in patients with DMG who received chemo- and/or radiotherapy.[32] Since we lack complete treatment status information for our current patient cohorts, this warrants caution to not overinterpret IGFS11-VISTA targeting as beneficial for every patient. However, our analysis of publicly available bulk RNA sequencing datasets shows uniformly high *IGSF11* expression across pediatric glioma cases. This provides rationale for neoadjuvant targeting of IGSF11, at a stage when brain-specific tumor immunity is still intact. Targeting IGSF11 as a first-line treatment before potential chemotherapy/radiotherapy-induced microglial depletion may, therefore, be most effective and seems considerable given the limited therapeutic benefit of current standard-of-care treatments.[76]

Altogether, we identify IGSF11 as a highly promising immunotherapy target for DMG, establishing a treatment axis that depends on harnessing the local brain-intrinsic immune system to target the tumor. The absence of systemic immune cell recruitment and activation – together with IGSF11's restricted expression pattern – supports a favorable safety profile encouraging further pre-clinical and clinical development.

RESOURCE AVAILABILITY

Lead contact

Further information and requests for resources and reagents should be directed to and will be fulfilled by the lead contact, Anne C. Rios (a.c.rios@prinsesmaximacentrum.nl).

Materials availability

This study did not generate new unique reagents.

Data and code availability

All newly generated SN sequencing and ST datasets are available on Zenodo: https://doi.org/10.5281/zenodo.17922773. Previously published DMG datasets re-analyzed in this study were retrieved from the following repositories: GEO: GSE210568, GSE194329, GSE280990, and BioStudies: E-MTAB-15147. This study did not generate any original code. Microscopy data reported in this study will be shared by the lead contact upon request.

ACKNOWLEDGMENTS

All imaging was performed at the Princess Máxima Imaging Center. We thank L. Sewing from the Princess Máxima Center Pathology Diagnostic Laboratory for the obtention of patient tumor samples and characterization. We thank all children and families that have contributed to this research through the Princess Máxima Center Tumor Donation Program. We thank Prof. Dr. Fritz Rathjen from the Max-Delbrück-Center Berlin for the gift of anti-Igsf11 antibody. This work was financially supported by the Princess Máxima Center for Pediatric Oncology and Oncode Institute, the Netherlands. R.C. and A.C.R were supported by an ERC-starting grant 2018 project (no. 804412).

AUTHOR CONTRIBUTIONS

Conceptualization, R.C., C.R.M., H.G.S., A.Z., and A.C.R.; resources, R.C., C.R.M., C.H., H.J., J.B., H.G.R., F.C.A.R., M.v.d.W., M.K., M.E.G.K., D.G.V., J.R.C., E.H., H.G.S., A.Z., and A.C.R.; investigation, R.C., C.R.M., C.H., T.J.M.v.B., D.K., A.K.L.W., H.C.R.A., H.J., B.M.T.V., A.J., J.B., E.B., H.G.R., B.M.P., and A.Z.; data curation, R.C., C.R.M., and A.Z., formal analysis and software; R.C., C.R.M., C.H., T.J.M.v.B., and R.L.v.I.; visualization, R.C., C.R.M., C.H., T.J.M.v.B., A.Z., and A.C.R.; writing, R.C., C.R.M., E.J.W., H.G.S., A.Z., and A.C.R.; supervision, P.A.R., H.G.S., A.Z., and A.C.R.; funding acquisition, A.C.R., H.G.S., and E.W.; project administration, A.C.R.

DECLARATION OF INTERESTS

A.Z. currently works at Genmab, The Netherlands. All other authors declare no competing interests.

STAR★METHODS

Detailed methods are provided in the online version of this paper and include the following:

- KEY RESOURCES TABLE
- EXPERIMENTAL MODEL AND STUDY PARTICIPANT DETAILS
    - Animal models
    - Human models
- METHOD DETAILS
    - Immunofluorescent imaging of 3D tissue
    - Cyclic immunofluorescence in 2D tissue sections
    - Image processing and spatial analysis
    - *Igsf11* shRNA knockdown, overexpression or knockout
    - Western Blot analysis
    - RT-qPCR analysis
    - CellTiter-Glo cell viability analysis
    - Proliferation curve
    - Bioluminescence imaging
    - Inducible Igsf11 knockdown spheroid generation
    - Inducible Igsf11 knockdown in immunocompetent mice
    - Microglia depletion in immunocompetent and -deficient mice
    - Tumor burden analysis
    - Mouse organotypic brain slice culture and antibody treatment
    - Brainstem organoid co-culture
    - DMG biopsy tissue fragment antibody treatment
    - Single nuclei RNA sequencing
    - Sample preparation and imaging for Visium
    - 10x Visium library generation and sequencing
    - Expression analyses of human pediatric brain tumors
    - Sequencing data processing and genome mapping
    - snRNA-seq data analysis
    - Cell type annotation and visualization techniques
    - Comparison of gene modules with public signatures
    - Cell-cell communication analysis
    - Analysis of Visium spatial transcriptomics data
    - Analysis of CosMx spatial transcriptomics data
    - Pathway activity inference and interaction analysis in spatial data
    - Statistical analysis

SUPPLEMENTAL INFORMATION

Supplemental information can be found online at https://doi.org/10.1016/j.ccell.2025.12.020.

Received: February 18, 2025
Revised: October 3, 2025
Accepted: December 23, 2025

REFERENCES

1. Schwartzentruber, J., Korshunov, A., Liu, X.-Y., Jones, D.T.W., Pfaff, E., Jacob, K., Sturm, D., Fontebasso, A.M., Quang, D.-A.K., Tönjes, M., et al. (2012). Driver mutations in histone H3.3 and chromatin remodelling genes in paediatric glioblastoma. Nature *482*, 226–231. https://doi.org/10.1038/nature10833.
2. Wu, G., Broniscer, A., McEachron, T.A., Lu, C., Paugh, B.S., Becksfort, J., Qu, C., Ding, L., Huether, R., Parker, M., et al. (2012). Somatic histone H3 alterations in pediatric diffuse intrinsic pontine gliomas and non-brainstem glioblastomas. Nat. Genet. *44*, 251–253. https://doi.org/10.1038/ng.1102.
3. Findlay, I.J., De Iuliis, G.N., Duchatel, R.J., Jackson, E.R., Vitanza, N.A., Cain, J.E., Waszak, S.M., and Dun, M.D. (2022). Pharmaco-proteogenomic profiling of pediatric diffuse midline glioma to inform future treatment strategies. Oncogene *41*, 461–475. https://doi.org/10.1038/s41388-021-02102-y.
4. Louis, D.N., Perry, A., Wesseling, P., Brat, D.J., Cree, I.A., Figarella-Branger, D., Hawkins, C., Ng, H.K., Pfister, S.M., Reifenberger, G., et al. (2021). The 2021 WHO Classification of Tumors of the Central Nervous System: a summary. Neuro Oncol. *23*, 1231–1251. https://doi.org/10.1093/neuonc/noab106.
5. Mackay, A., Burford, A., Carvalho, D., Izquierdo, E., Fazal-Salom, J., Taylor, K.R., Bjerke, L., Clarke, M., Vinci, M., Nandhabalan, M., et al. (2017). Integrated Molecular Meta-Analysis of 1,000 Pediatric High-Grade and Diffuse Intrinsic Pontine Glioma. Cancer Cell *32*, 520–537.e5. https://doi.org/10.1016/j.ccell.2017.08.017.
6. Filbin, M.G., Tirosh, I., Hovestadt, V., Shaw, M.L., Escalante, L.E., Mathewson, N.D., Neftel, C., Frank, N., Pelton, K., Hebert, C.M., et al. (2018). Developmental and oncogenic programs in H3K27M gliomas dissected by single-cell RNA-seq. Science *360*, 331–335. https://doi.org/10.1126/science.aao4750.
7. Liu, I., Jiang, L., Samuelsson, E.R., Marco Salas, S., Beck, A., Hack, O.A., Jeong, D., Shaw, M.L., Englinger, B., LaBelle, J., et al. (2022). The landscape of tumor cell states and spatial organization in H3-K27M mutant diffuse midline glioma across age and location. Nat. Genet. *54*, 1881–1894. https://doi.org/10.1038/s41588-022-01236-3.
8. Verhaak, R.G.W., Hoadley, K.A., Purdom, E., Wang, V., Qi, Y., Wilkerson, M.D., Miller, C.R., Ding, L., Golub, T., Mesirov, J.P., et al. (2010). Integrated Genomic Analysis Identifies Clinically Relevant Subtypes of Glioblastoma Characterized by Abnormalities in PDGFRA, IDH1, EGFR, and NF1. Cancer Cell *17*, 98–110. https://doi.org/10.1016/j.ccr.2009.12.020.
9. Neftel, C., Laffy, J., Filbin, M.G., Hara, T., Shore, M.E., Rahme, G.J., Richman, A.R., Silverbush, D., Shaw, M.L., Hebert, C.M., et al. (2019). An Integrative Model of Cellular States, Plasticity, and Genetics for Glioblastoma. Cell *178*, 835–849.e21. https://doi.org/10.1016/j.cell.2019.06.024.
10. Wang, Q., Hu, B., Hu, X., Kim, H., Squatrito, M., Scarpace, L., deCarvalho, A.C., Lyu, S., Li, P., Li, Y., et al. (2017). Tumor Evolution of Glioma-Intrinsic Gene Expression Subtypes Associates with Immunological Changes in the Microenvironment. Cancer Cell *32*, 42–56.e6. https://doi.org/10.1016/j.ccell.2017.06.003.
11. Nam, A.S., Chaligne, R., and Landau, D.A. (2021). Integrating genetic and non-genetic determinants of cancer evolution by single-cell multi-omics. Nat. Rev. Genet. *22*, 3–18. https://doi.org/10.1038/s41576-020-0265-5.
12. Venkatesh, H.S., Tam, L.T., Woo, P.J., Lennon, J., Nagaraja, S., Gillespie, S.M., Ni, J., Duveau, D.Y., Morris, P.J., Zhao, J.J., et al. (2017). Targeting neuronal activity-regulated neuroligin-3 dependency in high-grade glioma. Nature *549*, 533–537. https://doi.org/10.1038/nature24014.
13. Venkatesh, H.S., Johung, T.B., Caretti, V., Noll, A., Tang, Y., Nagaraja, S., Gibson, E.M., Mount, C.W., Polepalli, J., Mitra, S.S., et al. (2015). Neuronal Activity Promotes Glioma Growth through Neuroligin-3 Secretion. Cell *161*, 803–816. https://doi.org/10.1016/j.cell.2015.04.012.
14. Venkatesh, H.S., Morishita, W., Geraghty, A.C., Silverbush, D., Gillespie, S.M., Arzt, M., Tam, L.T., Espenel, C., Ponnuswami, A., Ni, L., et al. (2019). Electrical and synaptic integration of glioma into neural circuits. Nature *573*, 539–545. https://doi.org/10.1038/s41586-019-1563-y.
15. Venkataramani, V., Tanev, D.I., Strahle, C., Studier-Fischer, A., Fankhauser, L., Kessler, T., Körber, C., Kardorff, M., Ratliff, M., Xie, R., et al. (2019). Glutamatergic synaptic input to glioma cells drives brain tumour progression. Nature *573*, 532–538. https://doi.org/10.1038/s41586-019-1564-x.
16. Hara, T., Chanoch-Myers, R., Mathewson, N.D., Myskiw, C., Atta, L., Bussema, L., Eichhorn, S.W., Greenwald, A.C., Kinker, G.S., Rodman, C., et al. (2021). Interactions between cancer cells and immune cells drive transitions to mesenchymal-like states in glioblastoma. Cancer Cell *39*, 779–792.e11. https://doi.org/10.1016/j.ccell.2021.05.002.
17. Gangoso, E., Southgate, B., Bradley, L., Rus, S., Galvez-Cancino, F., McGivern, N., Güç, E., Kapourani, C.-A., Byron, A., Ferguson, K.M., et al. (2021). Glioblastomas acquire myeloid-affiliated transcriptional programs via epigenetic immunoediting to elicit immune evasion. Cell *184*, 2454–2470.e26. https://doi.org/10.1016/j.cell.2021.03.023.
18. Lin, G.L., Nagaraja, S., Filbin, M.G., Suvà, M.L., Vogel, H., and Monje, M. (2018). Non-inflammatory tumor microenvironment of diffuse intrinsic pontine glioma. Acta Neuropathol. Commun. *6*, 51. https://doi.org/10.1186/s40478-018-0553-x.
19. Lieberman, N.A.P., DeGolier, K., Kovar, H.M., Davis, A., Hoglund, V., Stevens, J., Winter, C., Deutsch, G., Furlan, S.N., Vitanza, N.A., et al. (2019). Characterization of the immune microenvironment of diffuse intrinsic pontine glioma: implications for development of immunotherapy. Neuro Oncol. *21*, 83–94. https://doi.org/10.1093/neuonc/noy145.
20. Andrade, A.F., Annett, A., Karimi, E., Topouza, D.G., Rezanejad, M., Liu, Y., McNicholas, M., Gonzalez Santiago, E.G., Llivichuzhca-Loja, D., Gehlhaar, A., et al. (2024). Immune landscape of oncohistone-mutant gliomas reveals diverse myeloid populations and tumor-promoting function. Nat. Commun. *15*, 7769. https://doi.org/10.1038/s41467-024-52096-w.
21. Jessa, S., Mohammadnia, A., Harutyunyan, A.S., Hulswit, M., Varadharajan, S., Lakkis, H., Kabir, N., Bashardanesh, Z., Hébert, S., Faury, D., et al. (2022). K27M in canonical and noncanonical H3 variants occurs in distinct oligodendroglial cell lineages in brain midline gliomas. Nat. Genet. *54*, 1865–1880. https://doi.org/10.1038/s41588-022-01205-w.
22. Ren, Y., Huang, Z., Zhou, L., Xiao, P., Song, J., He, P., Xie, C., Zhou, R., Li, M., Dong, X., et al. (2023). Spatial transcriptomics reveals niche-specific enrichment and vulnerabilities of radial glial stem-like cells in malignant gliomas. Nat. Commun. *14*, 1028. https://doi.org/10.1038/s41467-023-36707-6.
23. Kordowski, A., Mulay, O., Tan, X., Vo, T., Baumgartner, U., Maybury, M.K., Hassall, T., Harris, L., Nguyen, Q., and Day, B.W. (2025). Spatial analysis of a complete DIPG-infiltrated brainstem reveals novel ligand-receptor mediators of tumour-to-TME crosstalk. Acta Neuropathol. Commun. *13*, 35. https://doi.org/10.1186/s40478-025-01952-x.
24. Broek, T.J.M. van den, Hoogendijk, R., Kranendonk, M.E.G., Lammers, J.A.S., Krishnamoorthy, A.L., Ineveld, R.L. van, Molleson, M., Tsvetkov, V.O., Ringnalda, F.C.A., Wetering, M. van de, et al. (2025). Single-cell spatial analysis of pediatric high-grade glioma reveals a novel population of SPP1+/GPNMB+ myeloid cells with immunosuppressive and tumor-promoting capabilities. bioRxiv. https://doi.org/10.1093/neuped/wuaf002.
25. Moffet, J.J.D., Fatunla, O.E., Freytag, L., Kriel, J., Jones, J.J., Roberts-Thomson, S.J., Pavenko, A., Scoville, D.K., Zhang, L., Liang, Y., et al. (2023). Spatial architecture of high-grade glioma reveals tumor heterogeneity within distinct domains. Neurooncol. Adv. *5*, vdad142. https://doi.org/10.1093/noajnl/vdad142.
26. Ruiz-Moreno, C., Salas, S.M., Samuelsson, E., Minaeva, M., Ibarra, I., Grillo, M., Brandner, S., Roy, A., Forsberg-Nilsson, K., Kranendonk,

Please cite this article in press as: Collot et al., IGSF11-VISTA is a critical and targetable immune checkpoint axis in diffuse midline glioma, Cancer Cell (2025), https://doi.org/10.1016/j.ccell.2025.12.020

M.E.G., et al. (2025). Charting the single-cell and spatial landscape of IDH-wild-type glioblastoma with GBmap. Neuro Oncol. *27*, 2281–2295. https://doi.org/10.1093/neuonc/noaf113.

27. Hart, W.S., Myers, P.J., Purow, B.W., and Lazzara, M.J. (2024). Divergent transcriptomic signatures from putative mesenchymal stimuli in glioblastoma cells. Cancer Gene Ther. *31*, 851–860. https://doi.org/10.1038/s41417-023-00724-w.
28. Greenwald, A.C., Darnell, N.G., Hoefflin, R., Simkin, D., Mount, C.W., Gonzalez Castro, L.N., Harnik, Y., Dumont, S., Hirsch, D., Nomura, M., et al. (2024). Integrative spatial analysis reveals a multi-layered organization of glioblastoma. Cell *187*, 2485–2501.e26. https://doi.org/10.1016/j.cell.2024.03.029.
29. Galassi, C., Chan, T.A., Vitale, I., and Galluzzi, L. (2024). The hallmarks of cancer immune evasion. Cancer Cell *42*, 1825–1863. https://doi.org/10.1016/j.ccell.2024.09.010.
30. Kim, A.-R., Choi, S.J., Park, J., Kwon, M., Chowdhury, T., Yu, H.J., Kim, S., Kang, H., Kim, K.-M., Park, S.-H., et al. (2022). Spatial immune heterogeneity of hypoxia-induced exhausted features in high-grade glioma. OncoImmunology *11*, 2026019. https://doi.org/10.1080/2162402x.2022.2026019.
31. Sun, N., Victor, M.B., Park, Y.P., Xiong, X., Scannail, A.N., Leary, N., Prosper, S., Viswanathan, S., Luna, X., Boix, C.A., et al. (2023). Human microglial state dynamics in Alzheimer's disease progression. Cell *186*, 4386–4403.e29. https://doi.org/10.1016/j.cell.2023.08.037.
32. LaBelle, J.J., Haase, R.D., Beck, A., Haase, J., Jiang, L., Oliveira de Biagi, C.A., Jr., Neyazi, S., Englinger, B., Liu, I., Trissal, M., et al. (2025). Dissecting the immune landscape in pediatric high-grade glioma reveals cell state changes under therapeutic pressure. Cell Rep. Med. *6*, 102095. https://doi.org/10.1016/j.xcrm.2025.102095.
33. Depp, C., Doman, J.L., Hingerl, M., Xia, J., and Stevens, B. (2025). Microglia transcriptional states and their functional significance: Context drives diversity. Immunity *58*, 1052–1067. https://doi.org/10.1016/j.immuni.2025.04.009.
34. Mehta, N., Maddineni, S., Mathews, I.I., Andres Parra Sperberg, R., Huang, P.-S., and Cochran, J.R. (2019). Structure and Functional Binding Epitope of V-domain Ig Suppressor of T Cell Activation. Cell Rep. *28*, 2509–2516.e5. https://doi.org/10.1016/j.celrep.2019.07.073.
35. Wang, J., Wu, G., Manick, B., Hernandez, V., Renelt, M., Erickson, C., Guan, J., Singh, R., Rollins, S., Solorz, A., et al. (2019). VSIG-3 as a ligand of VISTA inhibits human T-cell function. Immunology *156*, 74–85. https://doi.org/10.1111/imm.13001.
36. ElTanbouly, M.A., Zhao, Y., Nowak, E., Li, J., Schaafsma, E., Le Mercier, I., Ceeraz, S., Lines, J.L., Peng, C., Carriere, C., et al. (2020). VISTA is a checkpoint regulator for naïve T cell quiescence and peripheral tolerance. Science *367*, eaay0524. https://doi.org/10.1126/science.aay0524.
37. Yoon, K.W., Byun, S., Kwon, E., Hwang, S.-Y., Chu, K., Hiraki, M., Jo, S.-H., Weins, A., Hakroush, S., Cebulla, A., et al. (2015). Control of signaling-mediated clearance of apoptotic cells by the tumor suppressor p53. Science *349*, 1261669. https://doi.org/10.1126/science.1261669.
38. Borggrewe, M., Kooistra, S.M., Noelle, R.J., Eggen, B.J.L., and Laman, J.D. (2020). Exploring the VISTA of microglia: immune checkpoints in CNS inflammation. J. Mol. Med. *98*, 1415–1430. https://doi.org/10.1007/s00109-020-01968-x.
39. Borggrewe, M., Grit, C., Den Dunnen, W.F.A., Burm, S.M., Bajramovic, J.J., Noelle, R.J., Eggen, B.J.L., and Laman, J.D. (2018). VISTA expression by microglia decreases during inflammation and is differentially regulated in CNS diseases. Glia *66*, 2645–2658. https://doi.org/10.1002/glia.23517.
40. Gholamin, S., Mitra, S.S., Feroze, A.H., Liu, J., Kahn, S.A., Zhang, M., Esparza, R., Richard, C., Ramaswamy, V., Remke, M., et al. (2017). Disrupting the CD47-SIRPα anti-phagocytic axis by a humanized anti-CD47 antibody is an efficacious treatment for malignant pediatric brain tumors. Sci. Transl. Med. *9*, eaaf2968. https://doi.org/10.1126/scitranslmed.aaf2968.
41. Pathania, M., De Jay, N., Maestro, N., Harutyunyan, A.S., Nitarska, J., Pahlavan, P., Henderson, S., Mikael, L.G., Richard-Londt, A., Zhang, Y., et al. (2017). H3.3K27M Cooperates with Trp53 Loss and PDGFRA Gain in Mouse Embryonic Neural Progenitor Cells to Induce Invasive High-Grade Gliomas. Cancer Cell *32*, 684–700.e9. https://doi.org/10.1016/j.ccell.2017.09.014.
42. Siddaway, R., and Hawkins, C. (2020). Modeling DIPG in the mouse brainstem. Neuro Oncol. *22*, 307–308. https://doi.org/10.1093/neuonc/noaa003.
43. Patel, S.K., Hartley, R.M., Wei, X., Furnish, R., Escobar-Riquelme, F., Bear, H., Choi, K., Fuller, C., and Phoenix, T.N. (2020). Generation of diffuse intrinsic pontine glioma mouse models by brainstem targeted in utero electroporation. Neuro Oncol. *22*, 381–392. https://doi.org/10.1093/neuonc/noz197.
44. Olmez, I., Love, S., Xiao, A., Manigat, L., Randolph, P., McKenna, B.D., Neal, B.P., Boroda, S., Li, M., Brenneman, B., et al. (2018). Targeting the mesenchymal subtype in glioblastoma and other cancers via inhibition of diacylglycerol kinase alpha. Neuro Oncol. *20*, 192–202. https://doi.org/10.1093/neuonc/nox119.
45. Ghouzlani, A., Rafii, S., Karkouri, M., Lakhdar, A., and Badou, A. (2020). The Promising IgSF11 Immune Checkpoint Is Highly Expressed in Advanced Human Gliomas and Associates to Poor Prognosis. Front. Oncol. *10*, 608609. https://doi.org/10.3389/fonc.2020.608609.
46. Tang, X.-Y., Xiong, Y.-L., Shi, X.-G., Zhao, Y.-B., Shi, A.-P., Zheng, K.-F., Liu, Y.-J., Jiang, T., Ma, N., and Zhao, J.-B. (2022). IGSF11 and VISTA: a pair of promising immune checkpoints in tumor immunotherapy. Biomark. Res. *10*, 49. https://doi.org/10.1186/s40364-022-00394-0.
47. Wanner, I.B., Anderson, M.A., Song, B., Levine, J., Fernandez, A., Gray-Thompson, Z., Ao, Y., and Sofroniew, M.V. (2013). Glial Scar Borders Are Formed by Newly Proliferated, Elongated Astrocytes That Interact to Corral Inflammatory and Fibrotic Cells via STAT3-Dependent Mechanisms after Spinal Cord Injury. J. Neurosci. *33*, 12870–12886. https://doi.org/10.1523/jneurosci.2121-13.2013.
48. Karve, I.P., Taylor, J.M., and Crack, P.J. (2016). Neuroinflammation and TBI. Br. J. Pharmacol. *173*, 692–702. https://doi.org/10.1111/bph.13125.
49. Chatinier, A. du, Meel, M.H., Das, A.I., Metselaar, D.S., Waranecki, P., Bugiani, M., Breur, M., Simonds, E.F., Lu, E.D., Weiss, W.A., et al. (2022). Generation of immunocompetent syngeneic allograft mouse models for pediatric diffuse midline glioma. Neuro-oncology Adv *4*, vdac079. https://doi.org/10.1093/noajnl/vdac079.
50. Mehta, N., Maddineni, S., Kelly, R.L., Lee, R.B., Hunter, S.A., Silberstein, J.L., Parra Sperberg, R.A., Miller, C.L., Rabe, A., Labanieh, L., and Cochran, J.R. (2020). An engineered antibody binds a distinct epitope and is a potent inhibitor of murine and human VISTA. Sci. Rep. *10*, 15171. https://doi.org/10.1038/s41598-020-71519-4.
51. Voabil, P., de Bruijn, M., Roelofsen, L.M., Hendriks, S.H., Brokamp, S., van den Braber, M., Broeks, A., Sanders, J., Herzig, P., Zippelius, A., et al. (2021). An ex vivo tumor fragment platform to dissect response to PD-1 blockade in cancer. Nat. Med. *27*, 1250–1261. https://doi.org/10.1038/s41591-021-01398-3.
52. Ito, M., Hiramatsu, H., Kobayashi, K., Suzue, K., Kawahata, M., Hioki, K., Ueyama, Y., Koyanagi, Y., Sugamura, K., Tsuji, K., et al. (2002). NOD/SCID/γc null mouse: an excellent recipient mouse model for engraftment of human cells. Blood *100*, 3175–3182. https://doi.org/10.1182/blood-2001-12-0207.
53. Shultz, L.D., Lyons, B.L., Burzenski, L.M., Gott, B., Chen, X., Chaleff, S., Kotb, M., Gillies, S.D., King, M., Mangada, J., et al. (2005). Human Lymphoid and Myeloid Cell Development in NOD/LtSz-scid IL2Rγnull Mice Engrafted with Mobilized Human Hemopoietic Stem Cells. J. Immunol. *174*, 6477–6489. https://doi.org/10.4049/jimmunol.174.10.6477.
54. Bowman, R.L., Klemm, F., Akkari, L., Pyonteck, S.M., Sevenich, L., Quail, D.F., Dhara, S., Simpson, K., Gardner, E.E., Iacobuzio-Donahue, C.A., et al. (2016). Macrophage Ontogeny Underlies Differences in Tumor-Specific Education in Brain Malignancies. Cell Rep. *17*, 2445–2459. https://doi.org/10.1016/j.celrep.2016.10.052.

55. Bessler, N., Wezenaar, A.K.L., Ariese, H.C.R., Honhoff, C., Dommann, N., Wehrens, E.J., Ruiz Moreno, C., van den Broek, T., Collot, R.V.U., Kloosterman, D.J., et al. (2026). De novo H3.3K27M-altered Diffuse Midline Glioma in human brainstem organoids to dissect GD2 CAR T cell function. Nature Cancer. https://doi.org/10.1038/s43018-025-01084-0.

56. Smyth, L.C.D., and Kipnis, J. (2025). Redefining CNS immune privilege. Nat. Rev. Immunol. *25*, 766–775. https://doi.org/10.1038/s41577-025-01175-0.

57. Butovsky, O., and Weiner, H.L. (2018). Microglial signatures and their role in health and disease. Nat. Rev. Neurosci. *19*, 622–635. https://doi.org/10.1038/s41583-018-0057-5.

58. Morini, R., Tagliatti, E., Bizzotto, M., and Matteoli, M. (2025). Microglial and TREM2 dialogues in the developing brain. Immunity *58*, 1068–1084. https://doi.org/10.1016/j.immuni.2025.04.022.

59. Geraghty, A.C., Acosta-Alvarez, L., Rotiroti, M.C., Dutton, S., O'Dea, M.R., Kim, W., Trivedi, V., Mancusi, R., Shamardani, K., Malacon, K., et al. (2025). Immunotherapy-related cognitive impairment after CAR T cell therapy in mice. Cell *188*, 3238–3258.e25. https://doi.org/10.1016/j.cell.2025.03.041.

60. Karimi, E., Yu, M.W., Maritan, S.M., Perus, L.J.M., Rezanejad, M., Sorin, M., Dankner, M., Fallah, P., Doré, S., Zuo, D., et al. (2023). Single-cell spatial immune landscapes of primary and metastatic brain tumours. Nature *614*, 555–563. https://doi.org/10.1038/s41586-022-05680-3.

61. Hambardzumyan, D., Gutmann, D.H., and Kettenmann, H. (2016). The role of microglia and macrophages in glioma maintenance and progression. Nat. Neurosci. *19*, 20–27. https://doi.org/10.1038/nn.4185.

62. Quail, D.F., and Joyce, J.A. (2017). The Microenvironmental Landscape of Brain Tumors. Cancer Cell *31*, 326–341. https://doi.org/10.1016/j.ccell.2017.02.009.

63. Kloosterman, D.J., and Akkari, L. (2023). Macrophages at the interface of the co-evolving cancer ecosystem. Cell *186*, 1627–1651. https://doi.org/10.1016/j.cell.2023.02.020.

64. Akkari, L., Gocheva, V., Quick, M.L., Kester, J.C., Spencer, A.K., Garfall, A.L., Bowman, R.L., and Joyce, J.A. (2016). Combined deletion of cathepsin protease family members reveals compensatory mechanisms in cancer. Genes Dev. *30*, 220–232. https://doi.org/10.1101/gad.270439.115.

65. Butowski, N., Colman, H., De Groot, J.F., Omuro, A.M., Nayak, L., Wen, P.Y., Cloughesy, T.F., Marimuthu, A., Haidar, S., Perry, A., et al. (2015). Orally administered colony stimulating factor 1 receptor inhibitor PLX3397 in recurrent glioblastoma: an Ivy Foundation Early Phase Clinical Trials Consortium phase II study. Neuro Oncol. *18*, 557–564. https://doi.org/10.1093/neuonc/nov245.

66. Suzu, S., Hayashi, Y., Harumi, T., Nomaguchi, K., Yamada, M., Hayasawa, H., and Motoyoshi, K. (2002). Molecular cloning of a novel immunoglobulin superfamily gene preferentially expressed by brain and testis. Biochem. Biophys. Res. Commun. *296*, 1215–1221. https://doi.org/10.1016/s0006-291x(02)02025-9.

67. Wu, C., Cao, X., and Zhang, X. (2021). VISTA inhibitors in cancer immunotherapy: a short perspective on recent progresses. RSC Med. Chem. *12*, 1672–1679. https://doi.org/10.1039/d1md00185j.

68. Ausejo-Mauleon, I., Labiano, S., de la Nava, D., Laspidea, V., Zalacain, M., Marrodán, L., García-Moure, M., González-Huarriz, M., Hervás-Corpión, I., Dhandapani, L., et al. (2023). TIM-3 blockade in diffuse intrinsic pontine glioma models promotes tumor regression and antitumor immune memory. Cancer Cell *41*, 1911–1926.e8. https://doi.org/10.1016/j.ccell.2023.09.001.

69. Mount, C.W., Majzner, R.G., Sundaresh, S., Arnold, E.P., Kadapakkam, M., Haile, S., Labanieh, L., Hulleman, E., Woo, P.J., Rietberg, S.P., et al. (2018). Potent antitumor efficacy of anti-GD2 CAR T cells in H3-K27M+ diffuse midline gliomas. Nat. Med. *24*, 572–579. https://doi.org/10.1038/s41591-018-0006-x.

70. Majzner, R.G., Ramakrishna, S., Yeom, K.W., Patel, S., Chinnasamy, H., Schultz, L.M., Richards, R.M., Jiang, L., Barsan, V., Mancusi, R., et al. (2022). GD2-CAR T cell therapy for H3K27M-mutated diffuse midline gliomas. Nature *603*, 934–941. https://doi.org/10.1038/s41586-022-04489-4.

71. Monje, M., Mahdi, J., Majzner, R., Yeom, K.W., Schultz, L.M., Richards, R.M., Barsan, V., Song, K.-W., Kamens, J., Baggott, C., et al. (2025). Intravenous and intracranial GD2-CAR T cells for H3K27M+ diffuse midline gliomas. Nature *637*, 708–715. https://doi.org/10.1038/s41586-024-08171-9.

72. Kloosterman, D.J., Erbani, J., Boon, M., Farber, M., Handgraaf, S.M., Ando-Kuri, M., Sánchez-López, E., Fontein, B., Mertz, M., Nieuwland, M., et al. (2024). Macrophage-mediated myelin recycling fuels brain cancer malignancy. Cell *187*, 5336–5356.e30. https://doi.org/10.1016/j.cell.2024.07.030.

73. Tam, W.L., and Weinberg, R.A. (2013). The epigenetics of epithelial-mesenchymal plasticity in cancer. Nat. Med. *19*, 1438–1449. https://doi.org/10.1038/nm.3336.

74. Lemoine, C., Da Veiga, M.A., Rogister, B., Piette, C., and Neirinckx, V. (2025). An integrated perspective on single-cell and spatial transcriptomic signatures in high-grade gliomas. npj Precis. Oncol. *9*, 44. https://doi.org/10.1038/s41698-025-00830-y.

75. Sattiraju, A., Kang, S., Giotti, B., Chen, Z., Marallano, V.J., Brusco, C., Ramakrishnan, A., Shen, L., Tsankov, A.M., Hambardzumyan, D., et al. (2023). Hypoxic niches attract and sequester tumor-associated macrophages and cytotoxic T cells and reprogram them for immunosuppression. Immunity *56*, 1825–1843.e6. https://doi.org/10.1016/j.immuni.2023.06.017.

76. Robison, N.J., and Kieran, M.W. (2014). Diffuse intrinsic pontine glioma: a reassessment. J. Neuro Oncol. *119*, 7–15. https://doi.org/10.1007/s11060-014-1448-8.

77. Ho, H., Fowle, A., Coetzee, M., Greger, I.H., and Watson, J.F. (2020). An inhalation anaesthesia approach for neonatal mice allowing streamlined stereotactic injection in the brain. J. Neurosci. Methods *342*, 108824. https://doi.org/10.1016/j.jneumeth.2020.108824.

78. Caretti, V., Jansen, M.H.A., van Vuurden, D.G., Lagerweij, T., Bugiani, M., Horsman, I., Wessels, H., van der Valk, P., Cloos, J., Noske, D.P., et al. (2013). Implementation of a multi-institutional diffuse intrinsic pontine glioma autopsy protocol and characterization of a primary cell culture. Neuropathol. Appl. Neurobiol. *39*, 426–436. https://doi.org/10.1111/j.1365-2990.2012.01294.x.

79. Feng, Y., Zheng, H., Tang, J., Li, X., Tian, R., and Ma, S. (2023). Protocol for generating in vitro glioma models using human-induced pluripotent- or embryonic-stem-cell-derived cerebral organoids. STAR Protoc. *4*, 102346. https://doi.org/10.1016/j.xpro.2023.102346.

80. Gutbier, S., Wanke, F., Dahm, N., Rümmelin, A., Zimmermann, S., Christensen, K., Köchl, F., Rautanen, A., Hatje, K., Geering, B., et al. (2020). Large-Scale Production of Human iPSC-Derived Macrophages for Drug Screening. Int. J. Mol. Sci. *21*, 4808. https://doi.org/10.3390/ijms21134808.

81. van Ineveld, R.L., Collot, R., Román, M.B., Pagliaro, A., Bessler, N., Ariese, H.C.R., Kleinnijenhuis, M., Kool, M., Alieva, M., Chuva de Sousa Lopes, S.M., et al. (2022). Multispectral confocal 3D imaging of intact healthy and tumor tissue using mLSR-3D. Nat. Protoc. *17*, 3028–3055. https://doi.org/10.1038/s41596-022-00739-x.

82. Watson, S.S., Duc, B., Kang, Z., de Tonnac, A., Eling, N., Font, L., Whitmarsh, T., Massara, M., and Bodenmiller, B. (2024). Microenvironmental reorganization in brain tumors following radiotherapy and recurrence revealed by hyperplexed immunofluorescence imaging. Nat. Commun. *15*, 3226. https://doi.org/10.1038/s41467-024-47185-9.

83. Windhager, J., Zanotelli, V.R.T., Schulz, D., Meyer, L., Daniel, M., Bodenmiller, B., and Eling, N. (2023). An end-to-end workflow for multiplexed image processing and analysis. Nat. Protoc. *18*, 3565–3613. https://doi.org/10.1038/s41596-023-00881-0.

84. Caretti, V., Sewing, A.C.P., Lagerweij, T., Schellen, P., Bugiani, M., Jansen, M.H.A., van Vuurden, D.G., Navis, A.C., Horsman, I., Vandertop, W.P., et al. (2014). Human pontine glioma cells can induce murine tumors.

Acta Neuropathol. *127*, 897–909. https://doi.org/10.1007/s00401-014-1272-4.

85. Yao, Z., Liu, H., Xie, F., Fischer, S., Adkins, R.S., Aldridge, A.I., Ament, S.A., Bartlett, A., Behrens, M.M., Van den Berge, K., et al. (2021). A transcriptomic and epigenomic cell atlas of the mouse primary motor cortex. Nature *598*, 103–110. https://doi.org/10.1038/s41586-021-03500-8.

86. Blanco-Carmona, E. (2022). Generating publication ready visualizations for Single Cell transcriptomics using SCpubr. Preprint at bioRxiv. https://doi.org/10.1101/2022.02.28.482303.

87. Bunis, D.G., Andrews, J., Fragiadakis, G.K., Burt, T.D., and Sirota, M. (2021). dittoSeq: universal user-friendly single-cell and bulk RNA sequencing visualization toolkit. Bioinformatics *36*, 5535–5536. https://doi.org/10.1093/bioinformatics/btaa1011.

88. Jin, S., Guerrero-Juarez, C.F., Zhang, L., Chang, I., Ramos, R., Kuan, C.-H., Myung, P., Plikus, M.V., and Nie, Q. (2021). Inference and analysis of cell-cell communication using CellChat. Nat. Commun. *12*, 1088. https://doi.org/10.1038/s41467-021-21246-9.

89. Abugessaisa, I., Ramilowski, J.A., Lizio, M., Severin, J., Hasegawa, A., Harshbarger, J., Kondo, A., Noguchi, S., Yip, C.W., Ooi, J.L.C., et al. (2021). FANTOM enters 20th year: expansion of transcriptomic atlases and functional annotation of non-coding RNAs. Nucleic Acids Res. *49*, D892–D898. https://doi.org/10.1093/nar/gkaa1054.

90. Wolf, F.A., Angerer, P., and Theis, F.J. (2018). SCANPY: large-scale single-cell gene expression data analysis. Genome Biol. *19*, 15. https://doi.org/10.1186/s13059-017-1382-0.

91. Palla, G., Spitzer, H., Klein, M., Fischer, D., Schaar, A.C., Kuemmerle, L.B., Rybakov, S., Ibarra, I.L., Holmberg, O., Virshup, I., et al. (2022). Squidpy: a scalable framework for spatial omics analysis. Nat. Methods *19*, 171–178. https://doi.org/10.1038/s41592-021-01358-2.

92. Kleshchevnikov, V., Shmatko, A., Dann, E., Aivazidis, A., King, H.W., Li, T., Elmentaite, R., Lomakin, A., Kedlian, V., Gayoso, A., et al. (2022). Cell2location maps fine-grained cell types in spatial transcriptomics. Nat. Biotechnol. *40*, 661–671. https://doi.org/10.1038/s41587-021-01139-4.

93. Cang, Z., Zhao, Y., Almet, A.A., Stabell, A., Ramos, R., Plikus, M.V., Atwood, S.X., and Nie, Q. (2023). Screening cell–cell communication in spatial transcriptomics via collective optimal transport. Nat. Methods *20*, 218–228. https://doi.org/10.1038/s41592-022-01728-4.

Please cite this article in press as: Collot et al., IGSF11-VISTA is a critical and targetable immune checkpoint axis in diffuse midline glioma, Cancer Cell (2025), https://doi.org/10.1016/j.ccell.2025.12.020

STAR★METHODS

KEY RESOURCES TABLE

REAGENT or RESOURCE	SOURCE	IDENTIFIER
Antibodies		
Rabbit anti-COL1 IgG antibody	Abcam	Cat# ab34710
Rat anti-CD45 IgG2b antibody	Biolegend	Cat# 103102; RRID: AB_312967
Rat anti-CD3 IgG2a antibody	Abcam	Cat# 33429; RRID: AB_726330
Rabbit anti-H3K27M IgG antibody	Thermo Fisher Scientific	Cat# MA5-27916; RRID: AB_2744969
Goat anti-IBA1 IgG antibody	Novus	Cat# NB100-1028; RRID: AB_521594
Chicken anti-GFAP IgY antibody	Abcam	Cat# ab4674; RRID: AB_304558
Rabbit anti-VISTA IgG antibody	Cell Signaling	Cat# 54979, RRID: AB_2799474
Mouse anti-TMEM119 IgG antibody	Cell Signaling	Cat# 41134
Mouse anti-CD49D IgG1k antibody	Thermo Fisher Scientific	Cat# 14-0499-82; RRID: AB_467292
Mouse anti-CD3 AF488 IgG1 antibody	Biolegend	Cat# 300454; RRID: AB_2564149
Rabbit anti-IGSF11 IgG antibody	Thermo Fisher Scientific	Cat# 703178
Rabbit anti-IGSF11 IgG antibody	Gift from Fritz G Rathjen, Max-Delbrück-Center for Molecular Biology, Berlin, Germany	Rb94, 95, 96
Rat anti-VISTA IgG2a antibody	Biolegend	Cat# 161302; RRID: AB_2876577
Rat anti-TREM2 IgG2b antibody	Biotechne	Cat# MAP17291
Mouse anti-CD206 IgG2b antibody	Biotechne	Cat# MAP25341
Mouse anti-GPNMB IgG1 antibody	Thermo Fisher Scientific	Cat# 12-9838-42; RRID: AB_2572736
Rabbit anti-CASPASE-3 IgG antibody	Cell Signaling	Cat# 9662; RRID: AB_331439
Mouse anti-GFAP IgG1 antibody	Cell signaling	Cat# 3670; RRID: AB_561049
Rat anti-KI67 IgG2a antibody	Thermo Fisher Scientific	Cat# 14-5698-82; RRID: AB_10854564
Goat anti-SPP1 IgG antibody	Biotechne	Cat# AF1433
Rat anti-CD31 IgG2a antibody	BD Biosciences	Cat# 553370; RRID: AB_396660
Human anti-F4/80 antibody	Miltenyi Biotec	Cat# 130-116-499; RRID: AB_2727574
Human anti-HLADR antibody	Miltenyi Biotec	Cat# 130-112-386; RRID: AB_2652902
Rabbit anti-CD4 IgG antibody	Abcam	Cat# ab133616; RRID: AB_2750883
SG7 mouse anti-VISTA IgG2A antibody	Laboratory of Jennifer Cochran	N/A
SG7 Human anti-VISTA IgG1K antibody	MedChemExpress	Cat# HY-P991447
Onvatilimab Human anti-VISTA IgG1K antibody	MedChemExpress	Cat# HY-P99040
Biological samples		
Human tissue samples were obtained from the Diffuse Midline Glioma Autopsy Program at the VU Medical Center and the Princess Máxima Center for Pediatric Oncology Tumor Donation Program (Máxima-TDP). All patient information is included in Table S1.	N/A	N/A
Chemicals, peptides, and recombinant proteins		
Pexidartinib Hydrochloride (PLX-3397)	MedChemExpress	Cat# HY-16749A
PEG400	MedChemExpress	Cat# HY-Y0873A
RM3 Doxycycline Hyclate	Tecnilab-BMI	Cat# E801700P01 0009
DAPI	Thermo Fisher Scientific	Cat# D3571; RRID: AB_2307445
Fast Green	Merch	Cat# F7252-5G
Fibroblast Growth Factor 2 (FGF2)	PeproTech	Cat# 100-18C
Dorsomorphin	Stem Cell Technologies	Cat# 72102

(*Continued on next page*)

Please cite this article in press as: Collot et al., IGSF11-VISTA is a critical and targetable immune checkpoint axis in diffuse midline glioma, Cancer Cell (2025), https://doi.org/10.1016/j.ccell.2025.12.020

Continued

REAGENT or RESOURCE	SOURCE	IDENTIFIER
CHIR99021	Stem Cell Technologies	Cat# 72052
SB431542	Stem Cell Technologies	Cat# 72232
Fibroblast Growth Factor 4 (FGF4)	Stem Cell Technologies	Cat# 78103.1
All-Trans Retinoic Acid	Stem Cell Technologies	Cat# 72262
Purmorphamine	Stem Cell Technologies	Cat# 72202
Matrigel	Corning	Cat# 354277
Vascular Endothelial Growth Factor (VEGF)	PeproTech	Cat# 100-20-100ug
Bone Morphogenetic Protein 4 (BMP4)	Stem Cell Technologies	Cat# 78211
Human Stem Cell Factor (human SCF)	Miltenyi Biotec	Cat# 130-093-991
Macrophage Colony Stimulating Factor (M-CSF)	PeproTech	Cat# 300-25-50ug
Interleukin-3 (IL-3)	PeproTech	Cat# AF-200-02-10ug
Low Melting Point (LMP) agarose	Invitrogen	Cat# 16520-050
Donkey serum	Merck	Cat# S30-100ml
Slowfade Gold Antifade	Invitrogen	Cat# S36936
Critical commercial assays		
Single Cell Gene Expression 3'v3.1	10xGenomics	Cat#PN-1000269
Visium Spatial Gene Expression Slide & Reagent Kit	10xGenomics	Cat#PN-1000187
Rneasy mini	QIAGEN	Cat#74104
Deposited data		
New snRNA sequencing and spatial transcriptomics data of human and mouse DMG samples	This paper	Zenodo: 10.5281/zenodo.17922773
Re-analyzed snRNA and spatial transcriptomics DMG datasets	N/A	GEO: GSE210568, GSE194329, GSE280990 and BioStudies: MTAB-15147
Experimental models: Cell lines		
Murine IUE DMG 24B7 spheroids	Gift from Esther Hulleman's group, Princess Máxima Center for Pediatric Oncology, Utrecht, the Netherlands. Generated by Timothy N Phoenix's lab, Cincinnati Children's Hospital Medical Center, Ohio, USA.	N/A
M354AAB-TO (BT093) patient-derived DMG spheroids	Gift from Hans Clevers' group, Princess Máxima Center for Pediatric Oncology, Utrecht, the Netherlands.	N/A
H9 human Embryonic Stem Cells (WA09)	WiCell	Cat# WAe009-A; RRID: CVCL_9773
Experimental models: Organisms/strains		
Mouse: Crl:CD1(ICR) (CD1)	Charles River	Strain# 022
Mouse: NOD.Cg-*Prkdc*^{scid} *Il2rg*^{tm1Wjl}/Szj (NSG)	Charles River	Strain# 614
Mouse: C57BL/6NCrl (C57BL/6)	Charles River	Strain# 475
Oligonucleotides		
Igsf11_mouse_fw_qPCR 5′-ACGCTCAAGCTACCTCCAACAG-3′	This paper	N/A
Igsf11_mouse_rev_qPCR 5′-AACCTGGAGGTCCAGCAGACAG-3′	This paper	N/A
ACTB_mouse_fw_qPCR 5′-CATTGCTGACAGGATGCAGAAGG-3′	This paper	N/A
ACTB_mouse_rv_qPCR 5′-TGCTGGAAGGTGGACAGTGAGG-3′	This paper	N/A
Human IGSF11 KO Guide 5′- TGACCATCCAAATGACATTG-3′	This paper	N/A

(*Continued on next page*)

Please cite this article in press as: Collot et al., IGSF11-VISTA is a critical and targetable immune checkpoint axis in diffuse midline glioma, Cancer Cell (2025), https://doi.org/10.1016/j.ccell.2025.12.020

Continued

REAGENT or RESOURCE	SOURCE	IDENTIFIER
Recombinant DNA		
PBCAG-H3.3K27M-Ires-eGFP	Laboratory of Dr. Timothy Phoenix	N/A
PBCAG-DNp53-Ires-Luciferase	Laboratory of Dr. Timothy Phoenix	N/A
PBCAG-Pdgfra^{D842V}-Ires-eGFP	Laboratory of Dr. Timothy Phoenix	N/A
PCAG-PBase	Laboratory of Dr. Timothy Phoenix	N/A
pCMV_AncBE4max	Addgene	Cat# 112094
pFYF1320	Addgene	Cat# 47511
SMARTvector inducible lentiviral shRNA#3 *Igsf11*	Horizon Discovery	Cat# V3SM11253-237665054
SMARTvector inducible lentiviral non-targeting shRNA control	Horizon Discovery	Cat# VSC11658
pPB[shRNA#1]-mCherry:T2A:Puro-U6>mIgsf11	Vector Builder	Cat# VB900125-1938pfy
pPB-mCherry/Puro-CAG>mIgsf11	Vector Builder	Cat# VB900145-1846vgx
Software and algorithms		
Seurat version 4.0	https://satijalab.org/seurat/	RRID: SCR_016341
DoubletFinder version 2.0.3	https://github.com/chris-mcginnis-ucsf/DoubletFinder	RRID: SCR_018771
Numbat version 1.2.3	https://github.com/kharchenkolab/numbat	RRID: SCR_019207
SeuratWrappers version 0.3.0	https://github.com/satijalab/seurat-wrappers	RRID: SCR_022555
SCpubR version 1.1.2	https://github.com/enblacar/SCpubr	RRID: SCR_021139
DittoSeq version 1.11.0	https://github.com/dtm2451/dittoSeq	N/A
CellChat version 1.6.1	https://github.com/sqjin/CellChat	RRID: SCR_021946
Scanpy version 1.9.3	https://scanpy.readthedocs.io/en/stable/	RRID: SCR_018139
Squidpy version 1.4.1	https://squidpy.readthedocs.io/en/stable/	RRID: SCR_026157
Cell2location version 0.1.3.	https://cell2location.readthedocs.io/en/latest/	RRID: SCR_024859
Tangram version 1.0	https://tangram-sc.readthedocs.io/en/latest/	N/A
CellCharter version 0.2.0	https://cellcharter.readthedocs.io/en/latest/#	N/A
decoupleR version 1.4.0	https://saezlab.github.io/decoupleR/	*RRID*: SCR_027127
Commot version 0.1.0	https://github.com/zcang/COMMOT	N/A
Python version 3.9	https://www.python.org	RRID: SCR_008394
Prism version v10.1.1	https://www.graphpad.com	RRID: SCR_002798
R version 4.0.2	https://www.r-project.org	RRID: SCR_001905

EXPERIMENTAL MODEL AND STUDY PARTICIPANT DETAILS

Animal models

In utero *electroporation DMG mouse model*

All murine experiments were conducted in compliance with the Animal Welfare Committee of the Princess Máxima Center and both local and international regulations. Mice were housed at 45-65% humidity, 20.5-23.5°C and 12-hour light/12-hour dark cycle, in either conventional or Specific Opportunist Pathogen Free (SOPF) conditions using individually ventilated cages and sterile food and water *ad libitum*. Time-pregnant CD1 mice were used for all experimental procedures. The *in utero* electroporation (IUE) method was performed following established protocols.[43] Briefly, a concentrated DNA mixture (1 μg/μL for each plasmid) supplemented with 0.05% Fast Green (Sigma) was injected into the fourth ventricle of embryos using a pulled glass capillary pipette. Injected embryos were electroporated by administering 5 square pulses (45 V, 50 ms pulses with 950 ms intervals) with the positive electrode towards the brain stem (BTX/Harvard Bioscience). Following electroporation, embryos were carefully returned to the abdominal cavity, incisions were sutured, and the mice were monitored until fully recovered. Post-electroporation, pups were regularly monitored for signs of symptoms associated with tumor development, such as altered gait, lethargy, and weight loss. Plasmids used in DNA mixture were a kind gift from Timothy Phoenix (Winkle College of Pharmacy, University of Cincinnati): PBCAG-H3.3K27M-Ires-eGFP, PBCAG-DNp53-Ires-Luciferase, PBCAG-Pdgfra^{D842V}-Ires-eGFP, PCAG-PBase.[43]

Cell lines and culture conditions

The murine DMG spheroid line 24B7 used in this study was a kind gift from the Hulleman group and generated by the lab of Timothy Phoenix using the same plasmid combination as described above (H3.3K27M, DNp53 and Pdgfra^{D842V}). Primary patient-derived

Please cite this article in press as: Collot et al., IGSF11-VISTA is a critical and targetable immune checkpoint axis in diffuse midline glioma, Cancer Cell (2025), https://doi.org/10.1016/j.ccell.2025.12.020

H3K27M-altered DMG line M354AAB-TO (BT093) was kindly provided by Hans Clevers' group from the Princess Máxima Center. DMG lines were cultured as previously described[24,49] and subjected to mycoplasma testing.

Secondary syngeneic allograft DMG model

DMG allograft tumors were generated by stereotactically injecting 24B7 murine DMG spheroids derived from the IUE model as previously described.[49] Neonatal C57BL/6N pups (P3-P5) were anesthetized using isoflurane/O2 inhalation and placed on a 3D printed mold[77] under a stereotactic frame. A solution of 300.000 single cells in 1.5 μL PBS were injected into the posterior pons region (3 mm posterior to lambda, 0 mm lateral to the sagittal suture, and 3.5 mm deep) using a 5 μL Hamilton micro syringe and at a rate of 2 μL/min. After injection, the Hamilton syringe was retracted, and the pup returned to the mother if breathing regularly and active. Allografted pups were regularly monitored for signs of symptoms associated with tumor development, such as altered gait, lethargy, and weight loss. Mice that did not show any signs of symptoms or did not reach humane endpoint 97-100 days after injections were sacrificed according to the end point of the relevant ethical mouse study protocol.

NSG allograft DMG model

DMG orthotopic tumors in immunocompromised NSG (NOD.Cg-Prkdcscid Il2rgtm1Wjl/SzJ) mice were generated following the same stereotactical procedure as described for the secondary syngeneic allograft model above.

Mice tissue collection

Mice used for imaging applications were put under deep anesthesia by intra peritoneal injection of pentobarbital before trans-cardiac perfusion with PBS and 4% paraformaldehyde (PFA) (pH 7.4) and tissue collection. For transcriptomic applications, mice were euthanized using CO_2 and brains were flash frozen before embedding in OCT (Sakura Finetek) and stored at -80°C until further use. Frozen tissue sections of 10um were obtained with a cryostat (LEICA Cryostar NX70) and used for downstream analyses (10x 3′v3 snRNAseq and 10x Visium ST).

Human models

Human tissue collection

Human tissue samples were obtained from the Diffuse Intrinsic Pontine Glioma Autopsy Program at the VU University Medical Center[78] and the Princess Máxima Center for Pediatric Oncology Tumor Donation Program (Máxima-TDP). This program has been approved by the Medical Research Ethics Committee (MREC) NedMec (MEC 22-589/PB22TUM) for patients passing away from a pediatric brain or solid tumor. Parents and children over the age of 12, if not incapacitated, signed informed consent for post-mortem tissue collection through full body and/or brain autopsy. Fresh tissues obtained for snRNA-seq and Visium spatial transcriptomic were flash frozen, embedded in OCT (Sakura Finetek) and stored at -80°C until sectioning. Frozen tissue sections of 10um were obtained with a cryostat (LEICA Cryostar NX70) and used for downstream analyses (10x 3′v3.1 snRNAseq, 10x Visium ST).

Brainstem organoid patterning

Brainstem-regionalized Organoids (BrOs) were generated from H9 human Embryonic Stem Cells (hESC, WA09, WiCell) as described in our previous work.[55] H9 cells were cultured according to Feng et al. (2023)[79] and routinely subjected to mycoplasma testing. In short, for Embryoid Body (EB) formation, 7000 H9 cells were added per well of an ultra-low attachment treated U-bottom 96-well plate (Greiner Bio-One) in 100 μl BASE medium (1:1 Advanced DMEM/F-12 (Gibco) and Neurobasal (Gibco), 1X GlutaMax (Gibco)), supplemented with 10 μM Y-27632 (ROCKi, AbMole BioScience) and 4 ng/ml Fibroblast Growth Factor 2 (FGF2, PeproTech). BrOs were incubated at 37°C with 5% CO_2 and medium was replaced every 2-3 days. In the first week, PATTERNING medium (BASE medium, 1X N2 (Gibco), 1 mg/ml Heparin Solution (Stem Cell Technologies)), supplemented with 1 μM Dorsomorphin (DM, Stem Cell Technologies), 10 μM SB431542 (SB43, Stem Cell Technologies), 3 μM CHIR99021 (CHIR, Stem Cell Technologies) was used. In the second week, PATTERNING medium, supplemented with 1 μM DM, 10 μM SB43, 3 μM CHIR 10 ng/ml Fibroblast Growth Factor 4 (FGF4, Stem Cell Technologies), 10 μM All-Trans Retinoic Acid (RA, Stem Cell Technologies) and 1 μM Purmorphamine (PMA, Stem Cell Technologies) was used. On day 11, BrOs were embedded in 12 μl Matrigel droplets (Corning) and transferred to a 12-well suspension plate (Greiner Bio-One). In the third week, PATTERNING medium, supplemented with 10 ng/ml FGF4. 10 μM RA, and 1 μM PMA was used. On day 17, the plate was placed on an orbital shaker. From day 21 onwards, MATURATION medium (BASE medium, 0.5X N2, 0.5X B27 without vitamin A (Gibco), and 1X Penicillin-Streptomycin (Pen-Strep, Gibco)) was used.

Primitive macrophage progenitor culture

Primitive macrophage progenitors (PMPs) were generated from H9 hESCs using an adjusted protocol.[80] In short, for EB formation, 7000 H9 cells were added per well of an ultra-low attachment treated U-bottom 96-well plate in 100 μl mTeSR+ medium (StemCell Technologies), supplemented with 50 μM ROCKi, 50 μM Bone Morphogenetic Protein 4 (BMP4, StemCell Technologies), 50 ng/ml Vascular Endothelial Growth Factor (VEGF, PeproTech) and 20 ng/ml human Stem Cell Factor (human SCF, Miltenyi). On day 4, EBs were transferred to a 6-well plate with X-VIVO 15 medium (Lonza), supplemented with 1X GlutaMax, 1X Pen-Strep, 100 ng/ml Macrophage Colony Stimulating Factor (M-CSF, PeproTech) and 25 ng/ml Interleukin-3 (IL-3, PeproTech). EBs were incubated at 37°C with 5% CO_2 and medium was replaced every week. After 3 weeks, the release of PMPs in the supernatant was observed.

METHOD DETAILS

Immunofluorescent imaging of 3D tissue

Murine and human (autopsy/biopsy/organoid) brain tissue containing DMG tumors were processed using the mLSR3D protocol, as previously described.[81] In brief, samples were fixed at 4°C overnight in 4% PFA (pH 7.4) and washed for 30 minutes in PBS-Tween.

Please cite this article in press as: Collot et al., IGSF11-VISTA is a critical and targetable immune checkpoint axis in diffuse midline glioma, Cancer Cell (2025), https://doi.org/10.1016/j.ccell.2025.12.020

Mouse brains were cut in thick sections using a vibratome (250-300 μm) (Leica VT 1200S), whereas autopsy and biopsy patient material was cut in smaller pieces using a scalpel (1-2 mm^3). Blocking was done using wash buffer 1 for 3-4 hours depending on the size of the tissue. After blocking, immunolabeling was performed, using nonlabelled primary antibodies of different species at 4°C overnight (key resources table), followed by washing in wash buffer 2 and a final incubation with fluorescently labeled secondary antibodies at 4°C overnight. Finally, tissue clearing was achieved with three consecutive incubations steps in FUnGI clearing agent of increasing concentration in PBS (33% and 66% FUnGI for 2h at room temperature, 100% overnight at 4°C). Images were captured using a Zeiss LSM880 or a Leica Stellaris confocal microscope.

Cyclic immunofluorescence in 2D tissue sections

Cyclic immunofluorescence is based on the protocol described in.[82] In brief, brain cryosections were removed from -80°C storage and air-dried for 30 minutes at room temperature (RT) prior to post-fixation in 4% PFA for 10 minutes. The tissue was rehydrated with 3 incubations in PBS for 5 minutes and quenched in PBS and 10mM glycine for 20 minutes. Sections were washed two additional times for 5 minutes in PBS and permeabilized using PBS supplemented with 0.2% Triton X-100 for 10 minutes at RT. A border was drawn around the tissue sections with a hydrophobic PAP pen and the sections were washed 3 more times in PBS for 2 minutes. After tissue pre-processing, the tissue was exposed to a blocking solution of 100 mM NH4Cl (ThermoFisher), 150 mM maleimide (Merck), and 10% donkey serum (Merck) in PBS for 1 hour at room temperature. Immunofluorescence staining was performed with a first round of primary antibody solution (key resources table) in 100 mM NH4Cl and 5% donkey serum in PBS, incubated in a humidified chamber on an orbital shaker for 2.5 hours at RT. Sections were washed 3 times in PBS for 5 minutes, before proceeding with incubation with a secondary antibody solution (100 mM NH4CL, 5% donkey Serum and DAPI in PBS) for 1 hour at RT and in the dark. A final round of washes (3x 5 minutes) in PBS was performed before proceeding with coverslip mounting in SlowFade Gold antifade mounting medium (Invitrogen). Samples were imaged on a Leica DMi8 Thunder imaging system using a 20x objective (NA 0.80, HC PL APO). To proceed to the next round of staining and imaging, the coverslips were allowed to slide off by gravity in a PBS bath and the sections were washed 3 additional times in fresh PBS for 5 minutes. Antibody removal was achieved using a chemical elution buffer containing 2 M urea, 40 mM tris(2-carboxyethyl)phosphine, 0.5 M glycine, and 3 M guanidium chloride in water for 3 minutes on the sections. A final wash (3x 5 minutes) in PBS was done before proceeding with the next staining cycle starting with blocking. Image analyses were performed in QuPath open software for bioimage analysis or MACS iQ View (Miltenyi Biotec).

Image processing and spatial analysis

Images were first merged using Leica LASX software. For co-registration of cyclic immunofluorescence (cIF) rounds, the DAPI channel served as a reference, and alignment was performed with the CycFluoCoreg tool developed by the Dream3DLab (https://github.com/Dream3DLab/CycFluoCoreg). The algorithm begins with an affine transformation to bring each channel into register with the DAPI reference, ensuring global alignment. This is then refined by applying a non-linear B-spline transformation to correct local distortions and improve channel overlap. Aligned images were subsequently imported into MACS iQ View for downstream processing. Tissue sections were run through nucleus detection and segmentation with a 3 μm cell expansion. Regions corresponding to tumor, tumor margin, exclusion areas, and non-tumor tissue were defined using the gating tools. Marker positivity was determined based on histogram X Range thresholds. Finally, spatial coordinates, intercellular distances, and marker intensities were exported and analyzed in R with the *imcRtools* package.[83]

Igsf11 shRNA knockdown, overexpression or knockout

Mouse IUE DMG 24B7 cells were electroporated with a piggy base shRNA construct pPB[shRNA#1]-mCherry:T2A:Puro-U6>mIgsf11 or pPB-mCherry/Puro-CAG>mIgsf11 purchased from Vector builder (VB900125-1938pfy and VB900145-1846vgx). Positive cells were selected with 0.5 mg/mL of puromycin (InvivoGen). Successful modulation of *Igsf11* expression was validated through Western Blot or qRT-PCR. IGSF11 knockout in human M354AAB-TO (BT093) DMG line was done using electroporation of a CRISPR Cas9 base editor (AncBE4max) and plasmid (pFYF1320) containing a guide RNA directed against Igsf11 (5′-TGACCATCCAAATGACATTG-3′).

Western Blot analysis

$0.5*10^6$-$1.5*10^6$ cells per sample were lysed in Laemmli protein buffer and treated with benzonuclease (Merck) for 30 minutes, prior to boiling. Extracted proteins were separated by SDS-PAGE and transferred to nitrocellulose membranes (AmershamBiosciences). After protein transfer, membranes were blocked for 1 hour in TBS-5% low fat milk (Elk, Campina) and stained overnight with primary antibodies Igsf11, 1:1000, and Vinculin 1:4000 (Sigma Aldrich) in TBS-1% milk powder (Campina), then washed in TBS-0.02% Tween, followed by IRDye conjugated secondary antibody staining for 45 minutes (Li-cor, Biotechnology). Proteins were visualized with the Odyssey®CLx (Li-cor, Biotechnology).

RT-qPCR analysis

Rneasy mini kit (QIAGEN) was used for RNA purification as described in the manufacturer's protocol. Complementary DNA (cDNA) conversion was performed using GoScript™ (Promega) and 600 ng of RNA per condition was converted according to the manufacturer's protocol. cDNA was then diluted to 1:4 ratio and final RNA expression levels were determined using the GoTaq® qPCR Master Mix (Promega) and gene-specific primers (key resources table).

Please cite this article in press as: Collot et al., IGSF11-VISTA is a critical and targetable immune checkpoint axis in diffuse midline glioma, Cancer Cell (2025), https://doi.org/10.1016/j.ccell.2025.12.020

CellTiter-Glo cell viability analysis

10.000 cells were seeded in a 96 well plate and cultured for 5 days with regular refreshing of the medium. Plates were analyzed following the manufacturer's protocol for CellTiter-Glo Luminescent Cell Viability Assay (Promega).

Proliferation curve

DMG cells were dissociated with Accutase (Innovative Cell Technologies), washed three times with PBS, and counted using a Countess™ automated cell counter (Invitrogen). A total of 100.000 cells were seeded per well in six-well plates and cultured for 3–4 days before harvesting and re-counting. At each passage, 100.000 cells were reseeded under the same conditions. Proliferation was quantified relative to the initial seeding density, and this procedure was repeated until day 9. Growth curves were generated based on the proliferation ratios calculated between consecutive time points.

Bioluminescence imaging

Tumor presence and growth monitoring was done using the *In Vivo* Imaging System (IVIS) Spectrum (Perkin Elmer) or the MILabs Optical Imaging Unit (U-OI). Five minutes before imaging, animals received an intraperitoneal injection of 150 mg/kg D-luciferin (ThermoFisher) and were anesthetized using isoflurane/O2 inhalation. Images were analyzed using the IVIS imaging software (Perkin Elmer) or OI-PP software (MILabs).

Inducible Igsf11 knockdown spheroid generation

Mouse IUE DMG 24B7 cells were transduced with a SMARTvector inducible lentiviral shRNA#3 targeting *Igsf11* (Horizon Discovery, V3SM11253-237665054) or with an inducible non-targeting shRNA control (Horizon Discovery, VSC11658). Transduced cells were selected with 0.5 mg/ml puromycin (InvivoGen). Expression of the shRNA was induced by addition of doxycycline (5 μg/ml), and knockdown efficiency was confirmed by RT-qPCR.

Inducible Igsf11 knockdown in immunocompetent mice

Secondary syngeneic allograft was done following the procedure described in the animal models section. 200 000 DOX inducible *Igsf11* KD (*Igsf11* shRNA) or control DMG cells (non-target shRNA) were injected in the pons of P3-P5 C57BL/6N mice (Charles River Laboratories, #475). After surgery, mice were monitored 3x per week by weighing and visual evaluation of clinical symptoms, such as weight loss, lack of grooming and/or immobility. 2 weeks after injection, mice were additionally monitored by bioluminescence imaging (BLI) weekly using a MILabs Optical Imaging Unit (U-OI). 2.5 weeks after injection, once a tumor is established as confirmed by BLI, the shRNA construct was continuously induced via RM3 food pellets containing 625 mg/kg Doxycycline Hyclate (Tecnilab-BMI, #E801700P01 0009). If humane or study endpoint was reached, mice were euthanized under deep anesthesia by intraperitoneal injection of 75 mg/kg ketamine and 1 mg/ml medetomidine, followed by trans-cardiac perfusion of PBS and/or Periodate-Lysine-Paraformaldehyde (PLP). Brains were collected for *ex vivo* analyses.

Microglia depletion in immunocompetent and -deficient mice

4-5 weeks old NSG (Charles River Laboratories, #614) and C57BL/6N mice were continuously treated with 600 mg/kg Pexidartinib Hydrochloride (PLX-3397, MedChemExpress, #HY-16749A) diluted in PEG400 (MedChemExpress, #HY-Y0873A) or only PEG400 in DietGel 93M cups (Bio-Services, #130023). After 1 week, 300 000 *Igsf11* KD or WT DMG cells were injected into the pons of 6-week-old mice based on previously published protocols by Caretti et al. (2014).[84] In short, mice received 0.067 mg/ml Carprofen in drinking water 24 hours before and 48 hours after surgery. In addition, 0.05 mg/kg buprenorphine was injected subcutaneously 30 minutes before surgery. Anesthesia was induced using 2.5% isoflurane/O2 inhalation, and mice were placed in a stereotaxic frame. 0.05% Lidocaine solution was applied topically to the cleaned surgical site before a 1 mm burr hole was drilled using a high-speed drill at the following coordinates: 0.8 mm posterior to lambda, 1 mm lateral to the sagittal suture, and 5 mm deep. Cells were injected using a 10-microliter syringe (Hamilton, #7635-01). After surgery, weight and discomfort were monitored daily for 72 hours, followed by monitoring 3x per week thereafter. Mice treated with PLX-3397 or vehicle and injected with *Igsf11* KD or WT DMG cells, were sacrificed at 20 days after injection. If humane or study endpoint was reached, mice were euthanized under deep anesthesia, followed by trans-cardiac perfusion, as previously described. Brains were collected for *ex vivo* analyses.

Tumor burden analysis

Fixed mouse brains were first imaged using a stereomicroscope (Leica M205) and subsequently embedded in 4% (w/v) low-melting-point agarose (in PBS) until set. Agarose-embedded brains were sectioned at 400 μm thickness using a vibratome (Leica VT1200S). All sections were examined for GFP signal under the stereomicroscope, and those containing signal were further imaged and quantified in Fiji. For quantification, background intensity was measured and subtracted, after which GFP-positive areas were identified by thresholding and the corresponding area was measured across all sections.

Mouse organotypic brain slice culture and antibody treatment

Tumor bearing mice were selected using BLI monitoring and euthanized under deep anesthesia, followed by trans-cardiac perfusion with PBS, as previously described. Brains were embedded in 4% (w/v) low-melting-point agarose prepared in ice-cold GBSS

Please cite this article in press as: Collot et al., IGSF11-VISTA is a critical and targetable immune checkpoint axis in diffuse midline glioma, Cancer Cell (2025), https://doi.org/10.1016/j.ccell.2025.12.020

containing 34.4 mM glucose and 1 mM kynurenic acid. Agarose blocks were trimmed and sectioned at 250 μm on a vibratome (Leica VT1200S) under sterile conditions. Brain slices were transferred onto Millicell (Merck) membrane inserts in six-well plates containing 1 ml of slice culture medium per well. The culture medium consisted of 25% MEM, 25% BME, 25% horse serum, 2 mM GlutaMAX, 1% penicillin–streptomycin, 34.4 mM glucose and 21.6% sterile water. The medium was adjusted to pH 7.2–7.4 and sterile-filtered before use. Cultures were maintained at 37°C in a humidified 5% CO_2 incubator. Medium was replaced daily during the first week of slice recovery period. Slices were treated during 5 days with either anti-Vista antibody (SG7, 10nM, J. Cochran Lab, Stanford) or Isotype control (mouse IgG2a, 10nM) in the culturing medium and refreshed once at day 3. To quantify tumor burden, the sections were imaged on a Leica DMi8 Thunder imaging system using a 10x objective (HC PL, NA 0.32) at beginning (Day 0) and end of the treatment (Day 5). Images were merged using Leica LASX software and tumor burden was quantified in Fiji as described above.

Brainstem organoid co-culture

Five-month-old BrOs were sectioned into 250 μm thick slices using a Leica VT 1200 S vibratome, transferred to a 48-well suspension plate (Greiner Bio-One) in 500 μl MATURATION medium, and incubated at 37°C with 5% CO_2 for 3 days. 200,000 PMPs, stained with DiI dye (1:1000, Thermo Fisher Scientific), were added per BrO slice for 7 days, before adding 50,000 *IGSF11* WT or KO M354AAB-TO (BT093) cells, stained with CellTracker Green (1:2000, Thermo Fisher Scientific). BrO slices were monitored using a Leica DMIL LED FLUO microscope with a 10X objective. After 24-72 hours, slices were fixed for imaging as previously described.

DMG biopsy tissue fragment antibody treatment

DMG biopsy patient material was cut in smaller pieces using a scalpel (1-2 mm^3). A 96-well plate was pre-coated with 40 μl of 4 mg/ml Matrigel per well. One tissue fragment was placed in each well and covered with an additional 40 μl Matrigel. After solidification, 100 μl medium (1:1 Advanced DMEM/F-12 and Neurobasal A (Gibco), 10 mM HEPES (Gibco), 1 mM Sodium Pyruvate (Gibco), 1X GlutaMax, 1x MEM Non-Essential Amino Acids (Gibco), 1:500 Primocin (InVivoGen), 1X B27 without vitamin A, 20 ng/ml EGF (PeproTech), 20 ng/ml FGF2, 10 ng/ml PDGF-AA (PeproTech), 10 ng/ml PDGF-BB (PeproTech), 2 μg/ml Heparin Solution), containing either 0.5 μM Onvatilimab (MedChemExpress), 10nM SG7 (MedChemExpress) or a human IgG1κ isotype control (InVivoMAb) was added. Medium was refreshed daily. After 72 hours, tissue fragments were fixed and cryosections of several areas throughout the fragments were cut. Staining and image acquisition were performed as previously described.

Single nuclei RNA sequencing

Several 10 um cryosections for each specimen were collected in an ice-cold tube and covered with 500 μL of cold lysis buffer 1 consisting of RNAse inhibitor and 0.1% NP40 in Tris-based buffer. After resuspension, the liquid was moved into a glass-on-glass dounce homogenizer on ice and homogenized with a loose and tight pestle for 10 and 15 strokes, respectively. The nuclei solution was filtered through a Flowmi cell strainer (70 μm, Bel-Art) and centrifuged at 4°C and 500g for 5 minutes. The pellet was gently resuspended with 1.5 mL of Wash Buffer (Tris-based buffer, 2% BSA, RNAse inhib.) and filtered through a 40um Flowmi strainer. Nuclei preparation was stained with DAPI and sorting of intact nuclei was done on a Sony SH800 cell sorter (Sony Biotechnology) using a 100 μm nozzle. Around 17000 nuclei per sample were directly sorted into 10x RT Buffer and immediately processed using the recommended protocol for nuclei capturing and library construction from the Single Cell Gene Expression 3'v3.1 (10x Genomics) kit. The resulting libraries were checked for quality on a 2100 Bioanalyzer (Agilent) and sequenced on a NovaSeq machine (Illumina).

Sample preparation and imaging for Visium

Brain tissue quality was assessed by sampling 5-10 frozen section of 10 μm and extracting RNA (Qiagen) before measuring RNA quality on an Agilent 2100 Bioanalyzer station. All murine and mouse samples with RIN values over 7 were used for 10x Visium spatial transcriptomics. A consecutive 10 μm section from the ones used for snRNA-seq was deposited on the Visium Spatial Gene Expression slide capture area, following the manufacturer's protocol. Tissue sections were stored at -80°C and further processed within 1 week. Sections were fixed in ice cold methanol for 30 minutes and stained using either an H3K27M primary antibody (1:400) or H&E for murine or human samples, respectively. Immunofluorescence and H&E stainings were performed according to the 10x Visium protocol (Methanol Fixation, Immunofluorescence/H&E Staining & Imaging for Visium Spatial Protocols CG000312/CG000160). Stained samples were imaged on an inverted brightfield microscope (Leica DMi8) using a 20x/0.8 NA dry objective and processed in the Leica Application Suite X software.

10x Visium library generation and sequencing

After imaging, Visium slides went through a first step of tissue permeabilization to release mRNA. Optimal permeabilization time (16 minutes) was previously determined using the Visium tissue optimization experiment kit. Finally, cDNA synthesis and library generation were done according to the manufacturer's protocol (Visium Spatial Gene Expression Slide & Reagent Kit). Library quality controls were done using the Agilent 2100 Bioanalyzer station and qRT-PCR (Milipore Sigma), before sequencing on the Novaseq platform (Illumina).

Expression analyses of human pediatric brain tumors

Gene expression profiles for various human pediatric brain tumors deposited in Gene Expression Omnibus under the identifiers GSE4290, GSE5675, GSE10327, GSE12992, GSE16011, GSE19348, GSE21687, GSE26576, GSE28026, GSE34771, GSE34824,

Please cite this article in press as: Collot et al., IGSF11-VISTA is a critical and targetable immune checkpoint axis in diffuse midline glioma, Cancer Cell (2025), https://doi.org/10.1016/j.ccell.2025.12.020

GSE35493, GSE36245, GSE37418, GSE44971, GSE49243, GSE49822, GSE64415, GSE70678, GSE73038, GSE74195, GSE100240, GSE122077, GSE122077 and GSE134404 were combined and analyzed using the R2 platform for genomic analysis and visualization (https://hgserver1.amc.nl/cgi-bin/r2/main.cgi).

Sequencing data processing and genome mapping

Sequencing output was handled by converting raw BCL files into FASTQ files utilizing the Cell Ranger mkfastq tool (version 6.0.0). Primary DMG samples underwent alignment against the human reference genome (Hg38), supplied by 10x Genomics. This was performed using Cell Ranger count, incorporating the include-introns flag to accurately enhance the gene expression profile capture of transcripts in single-nuclei data. For mouse samples relevant to our IUE experiments, we created a custom reference genome that integrated the sequences of transfected plasmid genes into the standard mouse genome (Mm10). This procedure was based on detailed protocols available on the 10x Genomics support site, ensuring alignment with specific modifications pertinent to our experimental design. Visium libraries were mapped using Space Ranger (version 1.1.0), a tool specifically tailored for processing spatially-resolved transcriptomic data provided by 10x Genomics.

snRNA-seq data analysis

Single-nucleus RNA-seq datasets from all experimental batches were processed using a standardized pipeline across both R and Python environments. Expression matrices were generated after alignment of raw FASTQ files to the GRCh38 reference genome (human samples) or to a custom mm10 reference containing the transfected plasmid sequences (IUE samples), ensuring uniform preprocessing across all datasets. For the human analysis, both newly generated DMG datasets and publicly available datasets (including Jessa et al.) were fully reprocessed under this same mapping strategy to avoid technical biases arising from heterogeneous pipelines. Initial data filtering was performed in Seurat (version 4.0), retaining genes expressed in at least five cells and nuclei with >200 detected genes and <10% mitochondrial reads to exclude low-quality or degraded nuclei. Doublets were identified and removed using DoubletFinder (version 2.0.3), with the expected multiplet rate adjusted according to 10x Genomics recovery estimates. Beyond *in silico* doublet removal, we further evaluated clusters in which cells expressed marker genes from two unrelated lineages. In such cases, careful assessment of gene expression signatures was performed, and if no consistent or biologically meaningful profile could be validated, these ambiguous populations were excluded from downstream analyses. Malignant cells in primary DMG samples were identified using the haplotype-aware CNV inference method numbat (version 1.2.3), whereas malignant nuclei in IUE samples were determined by the expression of reporter genes (eGFP or luciferase). Datasets were normalized and integrated using the fastMNN algorithm (SeuratWrappers version 0.3.0), harmonizing expression profiles across donors and studies. Dimensionality reduction was performed with Uniform Manifold Approximation and Projection (UMAP), followed by clustering using a shared nearest neighbor (SNN) graph approach with dataset-specific parameter tuning. Differential expression analysis was carried out using the Wilcoxon rank-sum test implemented in Seurat.

Cell type annotation and visualization techniques

Cell type identification utilized a multifaceted approach. Known gene signatures from both non-malignant and previously published malignant cell studies in DMG[6,7,85] were employed alongside reference mapping techniques implemented in Seurat. This dual approach allowed for robust cell-type annotation based on well-defined cellular phenotypes and pathological signatures, matching the expression of classical marker genes per cell type. Additional scoring of cells was conducted using the AddModuleScore function in Seurat, which assesses cell identity based on predefined gene modules. Visualization of complex datasets was achieved through various graphical representations, including stacked bar plots, dimensional reduction plots, and state plots created using SCpubR[86] (version 1.1.2) and DittoSeq[87] (version 1.11.0) tools, which facilitate the visual assessment of cellular compositions and gene expression dynamics across different sample conditions.

Comparison of gene modules with public signatures

To contextualize the transcriptional programs identified in DMG-associated microglia, we compared our differentially expressed gene (DEG) signatures with public gene signatures from NON-TUMOR contexts, which also included normal homeostatic microglia.[31] Overlap between gene sets was quantified using the Jaccard similarity coefficient, defined as the ratio of the intersection over the union of genes in each pairwise comparison. This metric provided a normalized measure of similarity between DMG-associated signatures and external reference signatures, facilitating cross-dataset comparisons of microglial activation states. Cross-species similarity was assessed at the marker level by mapping human DEGs to mouse orthologs using babelgene and then calculating the Jaccard similarity coefficient between human- and mouse-derived marker sets. This provided a normalized measure of overlap between the top subtype-specific markers in both species. To evaluate significance, we applied a hypergeometric test against the mouse gene universe with FDR correction.

Cell-cell communication analysis

To elucidate the intricate network of cell-cell communications within the DMG and IUE samples, the CellChat software (version 1.6.1)[88] was employed. This analysis was enriched by developing a custom L-R interaction database that merged the default 'CellChatDB.human' with additional interactions from the FANTOM5[89] resource. This enhancement allowed for a more comprehensive categorization of interaction pathways into groups, such as 'Secreted Signaling', 'ECM-Receptor Interaction', and 'Cell-Cell

Please cite this article in press as: Collot et al., IGSF11-VISTA is a critical and targetable immune checkpoint axis in diffuse midline glioma, Cancer Cell (2025), https://doi.org/10.1016/j.ccell.2025.12.020

Contact', broadening the scope of our communicative analysis. The adjusted database was utilized to calculate communication probabilities among different cell types, forming the basis for constructing weighted directed graphs that depict significant intercellular interactions. Intercellular communication networks are represented as weighted directed graphs that depict crucial interactions between cell populations. The strength of these interactions is quantified by the communication probability within the established communication pathways. To assess differences in interactions between human and mouse samples, we performed comparative analyses across multiple datasets that share similar cell-type compositions. This involved filtering out corresponding populations in each dataset to ensure a fair comparison of interaction dynamics. To further characterize the organization of the intercellular communication landscape, we applied the systems-level analysis framework implemented in CellChat. This approach integrates graph-theoretical measures, pattern recognition, and manifold learning to quantify and interpret signaling networks. Network centrality analysis was performed on weighted directed communication graphs to identify dominant senders (out-degree), receivers (in-degree), mediators (flow betweenness), and influencers (information centrality). In addition, CellChat was used to identify global communication patterns by factorizing outgoing and incoming signaling networks, thereby revealing how groups of cell types and signaling pathways coordinate to drive or respond to communication. The number of patterns was selected based on stability metrics.

Analysis of Visium spatial transcriptomics data

Analysis of spatial transcriptomics data from Visium experiments (this study, Ren et al. and Kordoski et al.)[22,23] was handled in Python using the Scanpy[90] (version 1.9.3) and Squidpy[91] (version 1.4.1) packages. This involved a series of preprocessing steps that included data importing, filtering based on total counts and expressed genes, and normalization. Dimensional reduction and clustering followed, identifying spatially variable features across the tissue samples. Cell types defined in both the IUE and human primary DMG samples were spatially mapped using the Bayesian model implemented in cell2location (version 0.1.3).[92] This tool not only determined the abundance of each cell type within each capture area of the Visium data but also facilitated the extraction of expression signatures using a negative binomial regression model. This model is particularly suited for robust integration of expression profiles across different technologies and batches. The spatial maps generated illustrate the estimated cell abundances of each cell type at a 5% quantile, ensuring confident assignment. Additionally, a non-negative matrix factorization (NMF) approach was applied to the absolute cell type abundance estimates per spot from cell2location, enabling the definition of distinct spatial compartments across the analyzed Visium samples.

Analysis of CosMx spatial transcriptomics data

CosMx high-plex RNA imaging datasets from van den Broek et al.[24] were reprocessed to investigate spatial cellular organization in DMG H3 K27–altered tissues. Negative-control probes were excluded, and quality control was applied to retain only fields of view (FOVs) corresponding to tumor tissue. Data were normalized and log-transformed using Scanpy (version 1.9.3). To transfer cell-type labels from our single-cell reference onto the CosMx dataset, we employed Tangram (version 1.0). The shared gene set between the CosMx panel and the reference atlas was identified and used for training in "single-cell mode." This yielded a mapping probability matrix linking single-cell transcriptomes to spatial voxels, from which Tangram projected cell-type annotations to each FOV. Mapping quality was evaluated by assessing training gene similarity scores, confirming adequate compatibility between the CosMx panel and the single-cell reference. To define multicellular spatial niches, we applied CellCharter (version 0.2.0). Latent embeddings were generated with scVI, accounting for sample-specific batch effects, and combined with graph-based spatial adjacency derived from Squidpy. CellCharter aggregated neighborhood features across multiple adjacency layers to construct enriched cell–context vectors. Stable niche partitions were identified by varying the number of clusters and selecting the solution with maximal stability. Finally, enrichment analyses were performed to determine the cell-type composition of each niche, based on Tangram-projected annotations.

Pathway activity inference and interaction analysis in spatial data

Pathway activity inference and enrichment of gene signatures within Visium datasets were performed using the decoupleR package (version 1.4.0) in Python, computing enrichment scores through Over Representation Analysis (ORA) based on public GO terms and curated signatures. To investigate spatially resolved cell–cell interactions, we applied spatial ligand–receptor inference with COMMOT (version 0.1.0[93];), which integrates gene expression with the spatial neighborhood graph of spots. Analyses were carried out using the CellChatDB ligand–receptor reference, enabling the inference of signaling interactions and their spatial propagation across malignant and immune compartments. COMMOT results were compared across datasets to identify reproducible communication patterns and tissue-specific differences.

Statistical analysis

Gene expression datasets were statistically analyzed using Mann-Whitney U test in Python (v3.9). Survival analysis was performed using a Mantel-Cox test and analysis of published mRNA expression datasets from human pediatric brain tumors using Kruskal-Wallis test with Dunn's correction to correct for multiple comparisons, both in Prism (v10.1.1). Protein expression and cell frequency in cIF imaging were compared using Student's T test in R Studio. Comparison of tumor burden was done using Dunn's multiple comparisons test in Prism (v10.1.1). ns $P > 0.05$; *$P < 0.05$; **$P < 0.01$; ***$P < 0.001$; ****$P < 0.0001$.